TECHNISCHE UNIVERSITÄT MÜNCHEN

Klinik für Kinderkardiologie und Angeborene Herzfehler

Deutsches Herzzentrum München des Freistaates Bayern

“Relative Pressure Gradients Across the Right Ventricular Outflow Tract Measured by Four-Dimensional Flow Cardiovascular Magnetic Resonance”

Piet Werner

Fakultät für Medizin

TECHNISCHE UNIVERSITÄT MÜNCHEN

Klinik für Kinderkardiologie und Angeborene Herzfehler

Relative Pressure Gradients Across the Right Ventricular Outflow Tract Measured by Four-Dimensional Flow Cardiovascular Magnetic Resonance

Piet Werner

Vollständiger Abdruck der von der
Fakultät für Medizin
der Technischen Universität München zur Erlangung des akademischen Grades
eines Doktors der Medizin
genehmigten Dissertation.

Vorsitzende/-r: Prof. Dr. Jürgen Schlegel

Prüfende/-r der Dissertation:

1. Prof. Dr. Peter Ewert

2. Prof. Dr. Adnan Kastrati

Die Dissertation wurde am 13.06.2019 bei der Technischen Universität München
eingereicht und durch die
Fakultät für Medizin am 01.01.2020 angenommen.

Contents

ABBREVIATIONS 4

1 INTRODUCTION 6

2 ROLE OF CARDIOVASCULAR MAGNETIC RESONANCE IN CONGENITAL HEART DISEASE 13

3 INTRODUCING MAGNETIC RESONANCE IMAGING 17

4 FOUR-DIMENSIONAL FLOW CARDIOVASCULAR MAGNETIC RESONANCE 25

5 PRESSURE GRADIENTS 32

6 AIM OF THE STUDY 36

7 METHODS 37

8 MATERIALS 45

8.1 Technical Equipment 45

8.2 Pharmaceuticals 46

9 RESULTS 47

9.1 Study Population 47

9.2 Cardiac Catheterization and Four-Dimensional Flow Cardiovascular Magnetic Resonance Measurements 51

9.3 Differences Between Cardiac Catheterization and Four-Dimensional Flow Cardiovascular Magnetic Resonance Measurements 56

9.4 Agreement Between Cardiac Cathertization and Four-Dimensional Flow Cardiovascular Magnetic Resonance Measurements 58

10 DISCUSSION 63

10.1 Limitations 69

10.2 Summary 72

10.3 Conclusion 74

11 ABSTRACT **75**

FIGURES **79**

TABLES **80**

REFERENCES **81**

Abbreviations

µg	microgram
2D	two-dimensional
3D	three-dimensional
4D	four-dimensional
ACHD	adult congenital heart disease
CC	cardiac catheterization
CT	computed tomography
CD-ROM	compact disc read-only memory
CFD	computational fluid dynamics
cGy	centigray
CHD	congenital heart disease or congenital heart defect
CI	confidence interval
CIED	cardiac implantable electronic devices
CIN	contrast-induced nephropathy
CINE	time-resolved images
CMR	cardiovascular magnetic resonance
deg.	degree
DICOM	digital imaging and communications in medicine
DORV	double outlet right ventricle
e.g.	exempli gratia or for example
ECG	electrocardiogram
et al.	et alia or and others
FT	Fourier transformation
g	gram
GRAPPA	generalized autocalibrating partially parallel acquisitions
HDIR	high dose ionizing radiation
Hz	hertz
ICD	implantable cardioverter defibrillator device
kg	kilogram
l	liter
LDIR	low dose ionizing radiation
LPA	left pulmonary artery
m	meter
mg	milligram
min	minute
ml	milliliter
mm	millimeter
mmHg	millimeter of mercury
mmol	millimole
MPA	main pulmonary artery

MR	magnetic resonance
MRI	magnetic resonance imaging
ms	millisecond
NMR	nuclear magnetic resonance
NSE	Navier-Stokes equations
Pa	pascal
PACS	picture archiving and communication system
PC MRA	time-averaged 3D PC MR angiogram
PC	phase contrast
pct.	percent
PDA	patent ductus arteriosus
PI	parallel imaging
PPE	Pressure Poisson equation
Qp:Qs	pulmonary to systemic flow volume rate ratio
RF	radiofrequency
ROI	region of interest
RPA	right pulmonary artery
RV	right ventricle
RVOT	right ventricular outflow tract
s	second
SD	standard deviation
SENSE	sensitivity encoding
TE	echo time
TGA	transposition of the great arteries
TOF	tetralogy of Fallot
TR	repetition time
TTE	transthoracic echocardiography
VENC	velocity-encoding value
VSD	ventricular septal defect

1 Introduction

Congenital heart disease (CHD) is the most common type of birth defect with an overall incidence of 75 per 1000 live births. Moderate and sever forms of CHD, which require expert cardiologic treatment, account for 6 per 1000 live births, newborns with bicuspid aortic valves not included (Hoffman & Kaplan, 2002). The overall prevalence for CHD in Germany accounts for 1.08% (Lindinger, Schwedler, & Hense, 2010).

CHD covers a broad spectrum of heterogeneous malformations of the cardiovascular system including nine groups, each with numerous independent diagnoses according to the 10th edition of International Classification of Diseases by the World Health Organization (WHO, 2016).

Over recent decades the life expectancy of patients with CHD has dramatically increased. Therefore, specialist societies had been encouraged to establish a new branch of cardiology named adults with congenital heart disease (ACHD), also referred to as grown-ups with congenital heart disease, since adults have exceeded children in prevalence for CHD. The decrease in mortality is a result of improvements in all fields that are necessary for the successful treatment of patients with CHD but mainly in cardiac surgery. Not only periprocedural patient care and invasive procedures are crucial for a better clinical outcome. It is also important to make a correct diagnose, select more suitable patients prior to procedures and carry out a long-term patient follow-up (Khairy et al., 2010; Marelli et al., 2014). Other factors may also play a role, like an increase in advanced prenatal diagnostics resulting in better care immediately after birth but also in termination of fetuses with most severe forms of CHD (Carvalho et al., 2004).

However, adult patients with CHD still have a higher mortality compared to the normal population, especially at younger age (Verheugt et al., 2010). Only those patients diagnosed with atrial septal defects and a patent ductus arteriosus are considered cured after the correction of the anatomical malformations (Nieminen, Jokinen, & Sairanen, 2007). CHD itself is the mortality cause with the highest prevalence in children suffering from CHD. Lesion severity and age at the time of surgery are significant predictors of survival in pediatric patients during the first year

after surgery (Chang, Rodriguez, Lee, & Klitzner, 2006). Congestive heart failure, by the majority a multifactorial emergence (Stout et al., 2016), and sudden cardiac death, predominantly induced by malignant arrhythmias (Koyak et al., 2012), are the most common causes of a CHD related death in adults (Engelings et al., 2016). With more than 80%, cardiovascular conditions are the most common reasons of a primary cause of death associated with hospitalization of adult CHD patients (Engelfriet et al., 2005). Beside a higher mortality attributable to CHD and subsequent cardiovascular conditions, patients with CHD have increased non-CHD related comorbidities, too (Nieminen et al., 2007).

Health professionals are often initially consulted when symptoms like shortness of breath occur for the first time. However, these symptoms may not become manifest until irreversible pathological processes have already been triggered. Therefore, to mitigate the clinical course of patients with CHD and to prevent consecutive comorbidities, it is important to perform a careful surveillance of the structural and functional status of the cardiovascular system before the onset of symptoms, to early detect hemodynamic and morphological as well as electrophysiological changes (Diller et al., 2005; Gratz, Hess, & Hager, 2009).

Apart from the medical history, physical examination, cardiopulmonary exercise testing and electrophysiological evaluation, imaging is paramount for a lifelong support of patients with CHD (Warnes et al., 2008). Due to the heterogeneity of the population with CHD and different strength and weaknesses of each imaging method, the individual patient can benefit from the application of multiple imaging modalities, which together should be sensitive, practical, reproducible, cost effective and at best non-harmful (Babu-Narayan, Giannakoulas, Valente, Li, & Gatzoulis, 2015).

The first-line investigation method for initial assessment and longitudinal evaluation of the anatomical as well as functional status of the heart and great vessels in CHD is transthoracic echocardiography (TTE). TTE comes along with an excellent spatial and temporal resolution of intracardiac structures, a broad availability, cost efficiency, the ability to measure hemodynamic parameters like blood flow velocity and the

consequential estimation of relative pressure gradients or absolute pressures in the right ventricle (RV). The diagnostic reliability of TTE in most forms of CHD can be high with a low percentage of major diagnostic errors in infants (Dorfman, Levine, Colan, & Geva, 2005). TTE is mainly limited by the acoustic window through coastal ribs, a restricted access to deeper body structures, compromised evaluation of complex lesions and compromised reevaluation after multiple invasive procedures. TTE has a relatively high observer-dependent variability due to an inaccurate positioning of the ultrasound beam related to blood flow and/or eventual miscalculation of cardiovascular geometries (Kupfahl et al., 2004; Wong, Spina, Toemoe, & Dhital, 2015).

For a long time, cardiac catheterization was essential to detect and comprehend pathophysiology mechanisms that are etiological for many cardiovascular conditions. Cardiac catheterization as a diagnostic tool might be indicated under the following broad circumstances: “First, […] to confirm or exclude the presence of a condition already suspected from history, physical examination, and/or noninvasive evaluation. Second, […] to clarify a confusing or obscure clinical picture in a patient, whose clinical findings and noninvasive data are inconclusive. Third, it is performed in some patients for whom corrective cardiac surgery is contemplated to confirm the suspected abnormality and to exclude associated abnormalities that might require the surgeon’s attention. Fourth, […] purely as a research procedure” (*Cardiovascular Catheterization and Intervention: A Textbook of Coronary, Peripheral, and Structural Heart Disease*, 2010).

Nowadays, cardiac catheterization should be reserved for interventions rather than the routine determination of the hemodynamic status quo because of well-established and less harmful alternatives (Nishimura & Carabello, 2012). Nevertheless, cardiac catheterization is the reverence diagnostic tool for angiography and hemodynamic evaluation. In clinical diagnostics of CHD, cardiac catheterization is indicated to calculate pulmonary resistance and absolute pressure gradients. Moreover, it is used to assess coronary arteries, pulmonary atresia, graft vasculopathy, collateral vessels and shunts through oximetry and/or flow ratios,

inconclusive findings after non-invasive imaging or in other less frequent situations such as biopsies (Feltes et al., 2011).

In order to protect the patient from a higher risk of cancer, diseases other than cancer and heritable germ line mutations caused by stochastic effects of low dose ionizing radiation[1] (LDIR) (UNSCEAR, 2012), the treating physician should carefully balance risks and benefits when considering a non-therapeutic cardiac catheterization procedure, to minimize radiation exposure following the "as low as reasonably achievable" principle (Mathews et al., 2013). This is especially important for neonates undergoing surgery, patients with genetic syndromes or severe CHD. It has been reported that the overall exposure to radiation in these subsets come to > 20 mSv/year compared to < 3 mSv/year affecting most patients with CHD (Glatz et al., 2014). Johnson and colleagues published data which display a median cumulative LDIR exposure per patient in their CHD study cohort of 2.7 mSv, although with a wide range of 0.1 to 76.9 mSv and higher effective doses reported for those with more complex cardiac anomalies. Additionally, "[m]edian lifetime attributable risk of cancer ranged widely […] and was twice as high in females per unit exposure (0.04% versus 0.02% per 1 mSv effective dose […])" (J. N. Johnson et al., 2014).

The fact of a higher susceptibility of radiation induced leukemia and certain types of solid cancer in children is well recognized, since age at exposure is an important determinant of malignancy risk associated with LDIR (ICRP, 2015; Preston et al., 2007). This needs to be emphasized as more than 80% of patients with CHD undergo a diagnostic and/or therapeutic cardiac catheterization procedure at ≤ 18 years of age. Of this group even more than 25% are ≤ 1 year of age (Jayaram et al., 2015). From 1990 until 2005 the median age at first LDIR exposure of children with CHD dropped from 5 years to 9.6 months. In the same period patients have been exposed increasingly to either diagnostic or therapeutic LDIR-related procedures. The three-year procedure rates of all modalities per 1000 patients have doubled from 58.1 to 119.2 within that time span. Diagnostic cardiac catheterization contributes with 44.1 procedures per

[1] ≤ 100 mSv

1000 patients. Therefore, diagnostic cardiac catheterization accounts for the biggest rate of all LDIR-related procedures. Additionally, therapeutic or interventional cardiac catheterization is the fastest growing LDIR emitting modality in CHD (Beausejour Ladouceur et al., 2016).

It appears that there is no radiation threshold beneath which stochastic effects do not occur (Monson et al., 2006). On the contrary, tissue reactions like skin erythema, formerly known as deterministic effects, do have a threshold. At the same time, the degree of severity of tissue reactions is directly proportional to radiation exposure (ICRP, 2012). Although the majority of international bodies base their radiation protection recommendations on the linear-no-threshold model, "managing radiation risk commensurate with a precautionary principle" (ICRP, 2015), other dose response models for LDIR exposure cannot be ruled out and the topic remains controversial (Tubiana, 2005). Some research groups even proclaim a beneficial effect for LDIR exposure in non-human research models (Calabrese, 2013).

Recent studies about gene expression alterations in human cells as a response to LDIR suggest that these alterations on biomolecular levels might differ not only quantitatively but also qualitatively from high dose ionizing radiation[2] (HDIR) exposure. Some alterations caused by LDIR maybe prosurvival compared to those following HDIR. However, it is also imaginable that exposed cells carry a risk of increased mutation load, potentially leading to carcinogenesis (Sokolov & Neumann, 2016). Generally speaking, negative or positive effects of LDIR or LDIR rates on exposed tissues depend on sex, age, genetic background, acute or chronic irradiation and type of irradiation (Tang, Loke, & Khoo, 2017).

Apart from the negative impact of fluoroscopy, cardiac catheterization might have immediate negative consequences for the patient as well. Adverse events of high severity can occur in up to 5% of CHD related diagnostic cardiac catheterization procedures (Bergersen et al., 2010).

Because of a high spatial resolution, cardiac computed tomography (CT) is mostly employed for comprehensive and complementary anatomical studies. Apart from cardiac catheterization, it is the imaging modality with

[2] > 100 mSv

the highest accuracy of the assessment of coronary artery anomalies in patients with CHD. Also, cardiac CT is a reasonable method to investigate lung parenchyma, airway anatomy and extracardiac structures. Newest scanners are capable to acquire images within one heartbeat and are therefore particularly suitable to evaluate hemodynamic instable patients with a suspected pulmonary embolism or the like. Cardiac CT especially comes into play when non-radiating imaging modalities are contraindicated or have a lower sensitivity and/or specificity for the clinical question of interest.

As stated above, cardiac CT is obviously unattractive for serial measurements due to LDIR exposure. Cardiac CT "should be reserved for situations in which it is expected to provide unique diagnostic information for the individual patient or clinical indication and/or less risk than other modalities" (Han et al., 2015).

Iodinated contrast agents enable and/or greatly enhance the diagnostic capabilities of cardiac catheterization as well as cardiac CT. Iodinated contrast agents can lead to Iodinated contrast agent induced postcontrast acute kidney injury or contrast-induced nephropathy (CIN). Adult patients with an impaired kidney function at eGFR < 45 ml/min/1.73m^2 are at a higher risk to develop CIN (Davenport, Khalatbari, Cohan, & Ellis, 2013). "Risk factors for CIN in children are thought to be similar to those in adults" (Ellis et al., 2015).

Iodinated contrast agents can lead to acute thyrotoxicosis in autonomous/autoimmune hyperthyroid patients, too.

Another way to not only evaluate morphology, but also functionality of the cardiovascular system, comes in the form of cardiovascular magnetic resonance (CMR). In 1973, Paul Lauterbur produced the first zeugmatographic image of an object composed of two thin glass capillaries of water inside a bigger glass tube filled with heavy water. Lauterbur used the varying nuclear magnetic resonance (NMR) of the two substances in interaction with magnetic field gradients to acquire two-dimensional (2D) spatial information. He points out that the new technique "should find many useful applications in studies of the internal structures, states and compositions of microscopic objects" (Lauterbur, 1973).

Today, it is possible to investigate a moving structure like the heart inside the human body based on the same principle.

2 Role of Cardiovascular Magnetic Resonance in Congenital Heart Disease

Since NMR was used for the first time to create a plane image of an object, CMR has made its way into guidelines for the management of CHD and ACHD as an imaging modality with various diagnostic workup applications. CMR is the reference method for blood flow and ventricular function measurements. It complements other modalities, is rarely used exclusively and especially helps to examine patients with complicated lesions. CMR provides a non-invasive, reproducible, unrestricted access to cardiovascular anatomy and physiology, without a negative impact on the integrity of human deoxyribonucleic acid (Fatahi et al., 2016).

Steady improvements, regarding the hard- and software in the field of CMR, have made magnetic resonance imaging (MRI) even more competitive compared to other imaging modalities in many aspects of CHD over the last decade. Handling CMR in CHD requires a great expertise in pediatrics, cardiology and magnetic resonance (MR) application particularly when anatomy is small, heart rates are high and clinical questions are complex (Valsangiacomo Buechel et al., 2015).

CMR is the leading diagnostic tool to quantify flow, shunts, right ventricular function, pulmonary valve regurgitation, right ventricular outflow tract (RVOT) obstruction and biventricular mass as well as tissue characterization, perfusion and fibrosis studies included. In comparison with TTE, CMR is inferior in investigating pulmonary artery pressure and small, extremely mobile structures such as valvular vegetations associated with endocarditis. Compared to cardiac CT, CMR is inferior in evaluating vessel collaterals, arteriovenous malformations, coronary anomalies, and coronary artery disease as well as extracardiac masses (Baumgartner et al., 2010). In opposition to cardiac catheterization, CMR is not capable to calculate pulmonary vascular resistance and to measure absolute blood pressure values. Moreover, CMR is inferior in evaluating coronary arteries compared to cardiac catheterization (Montalescot et al., 2013).

CMR limitations in general include availability, higher costs, time exposure, noise, compliance especially of children and cognitively

impaired patients, artefacts from stainless steel implants and claustrophobia not responding to preexamination anxiolytic medication. Additionally, CMR is limited by chronic kidney disease of higher grades, a condition associated with gadolinium-induced fibrosis respectively nephrogenic systemic fibrosis, caused by high doses and/or frequent applications of gadolinium-based contrast agents (Todd & Kay, 2016). Additionally, CMR is affected by thermal injuries caused by radiofrequency (RF) pulses as well as induced voltages from rapidly changing magnetic field gradients, along with high field strengths, in electrically conductive materials inside the scanner gantry (Shellock, 2000).

CMR is relatively contraindicated for non-MRI conditional cardiac pacemakers, implantable cardioverter defibrillator devices (ICDs), insertable cardiac monitors and cardiac resynchronization therapy devices, summarized under the term cardiac implantable electronic devices (CIEDs) (Grainger, 2014).

Arrhythmias represent a frequent and serious comorbidity in patients with CHD (Kaemmerer et al., 2008). With an aging CHD population arrhythmias also become more and more prevalent (Walsh & Cecchin, 2007). Therapy of arrhythmias is shifting from non-operative pharmacological treatment towards catheter ablation and CIED implantation (Khairy et al., 2014). A small but constant increase of insertion rates for pacemakers and ICDs in patients with CHD has been reported (Beausejour Ladouceur et al., 2016). With a simultaneously growing prevalence of CIEDs and increasing use of CMR in patients with CHD, the probability is rising that CMR is found to be useful to investigate this patient group (Fratz et al., 2013).

Three main mechanisms stand behind the concern that CIEDs could not be safe during CMR. First, magnetic fields causing attractive forces. Second, energy from RF pulses causing heat damage. Third, rapidly changing magnetic field gradients inducing electrical currents. Briefly summarized, these mechanisms might cause dangerous device malfunctions, tissue damage or both (Schaefer, Bourland, & Nyenhuis, 2000; Schenck, 2000).

MRI safety screening forms help to screen patients for CIEDs as well as ferromagnetic objects before examinations. When the patient's history is incomplete or not reliable in terms of cardiac procedures, a chest x-ray can be performed to identify CIEDs in situ. Communication with the physician maintaining the CIED and the device manufacturing company is elementary to approve whether the CIED is MR conditional or not. Checklists and manuals are endorsed to ensure the right handling of MR conditional and non-MR conditional CIEDs while the patient is exposed to the magnetic field during a scan (Kanal et al., 2013).

Patients with pacemaker-dependent non-MR conditional ICDs, CIEDs implanted before 2002, abandoned leads and CIEDs implanted in abdominal position are not included into the MagnaSafe study group by Russo and colleagues (Russo, 2013). They form the population with the highest risk for inadequate resynchronization, pacing or failing tachycardia therapy during CMR and should undergo alternative imaging if possible (Lowe, Plummer, Manisty, & Linker, 2015). It has been demonstrated that CMR can be performed without adverse events even in presence of abandoned leads and pacemaker dependent CIEDs (Horwood et al., 2016). It is to be expected that patients, who are excluded from CMR protocols today, will be found eligible for those by guideline panels within the next years (Nazarian et al., 2017; Russo et al., 2017).

CMR can be performed in patients with non-MR conditional CIEDs if no alternative method is available to acquire the additional information that might have the impact to escalate or deescalate the patient's clinical management. Patients with non-MR conditional CIEDs need to be informed that the planed procedure has an increased risk for life-threatening arrhythmias and serious device malfunction requiring a device replacement. A signed consent is mandatory as it is for every patient undergoing a CMR examination. General precautions for MR procedures with CIEDs include preimaging device reprogramming. Precautions also include patient monitoring, provision of resuscitation equipment, technical capability of transcutaneous pacing and presence of an interdisciplinary team of cardio- and radiologists (Grainger, 2014; Kanal et al., 2013).

Every patient with implanted wires/leads, functional metallic devices other than CIEDs or intracranial vascular clips needs to be reviewed with a risk benefit assessment and cleared by an attending radiologist before access to the scanner can be justified. Any kind of ferromagnetic implant (e.g. cochlea implants, neurostimulators, catheters, artificial valves and the like) is at risk of causing harm if RF pulses and/or rapidly changing magnetic field gradients are delivered over the region where the foreign object has been placed in vivo (Grainger, 2014; Kanal et al., 2013).

3 Introducing Magnetic Resonance Imaging

The NMR signal is generated by atomic nuclei with an uneven number of protons and/or neutrons exposed to an external magnetic field. Every atomic nucleus with an uneven number of protons and/or neutrons has a so called non-zero spin, such as a $_1H$ hydrogen isotope respectively proton as part of a water molecule. Nuclei with non-zero spins have at least two quantum mechanic properties. First, a magnetic moment and second, an angular momentum (Brown, Cheng, Haacke, Thompson, & Venkatesan, 2014).

The magnetic moment of spins can be described as a vector with orientation and length, also referred to as magnitude. Each spin vector can be decomposed into a longitudinal and transverse spin component vector. Furthermore, spin component vector magnitudes add up or cancel each other out depending on their orientation. Every $_1H$ hydrogen isotope outside of the scanner gantry has a spin vector of the same magnitude but random orientation due to thermal motion. Because of their random orientation, spin component vector magnitudes sum up to zero, which means there is no measurable macroscopic magnetization of a sample of $_1H$ hydrogen isotopes in absences of an external magnetic field (Brown et al., 2014).

Spin vectors are forced to align in the presence of an external magnetic field, since they can be described as permanent magnets. Now, the alignment of spin vectors is no longer random but not perfectly parallel or antiparallel to the external magnetic field lines. Spins experience at least two mechanical torques in the presence of an external magnetic field. First, a longitudinal created by the external magnetic field and second, a transverse due to the angular momentum. Hence, each spin aligns in a cone shaped trajectory with a rotating transverse spin component vector in addition to a static longitudinal spin component vector, parallel or antiparallel to the magnetic field lines. Consequently, spins are rotating respectively precessing around the axis of the external magnetic field (Brown et al., 2014).

The frequency of precession, called Larmor frequency, is proportional to the field strength of the external magnetic field, multiplied with a specific factor for each type of isotope, known as the gyromagnetic ratio.

Therefore, every proton as part of a water molecule in a completely homogenous external magnetic field is precessing with the same Larmor frequency (Brown et al., 2014).

Spins, which hold the same gyromagnetic ratio, may precess with the same frequency in a complete homogenous external magnetic field but they do not precess in phase. This means, each $_1H$ hydrogen isotope is precessing around the external magnetic field lines with $42.577 \times 10_6$ Hz/Tesla. However, the moment a $_1H$ hydrogen isotope passes the meter every $42.577 \times 10_6$ times per second is individual. Precisely said, transverse spin component vectors of $_1H$ hydrogen isotopes are running in a plane like the hands of a clock, each with any possible phase angle between 0 and 360 degrees. Because there is no phase coherency, transverse spin component vectors cancel each other out and leave no transverse magnetization to measure (Brown et al., 2014).

Since longitudinal spin component vectors are aligned parallel or antiparallel along the external magnetic field, magnitudes of longitudinal spin component vectors can be added up. In a simplified model, the parallel orientation is energetically more preferable for spins to take. According to this, a small relative excess in favor of the parallel orientation does exist in a sample of protons placed inside the scanner gantry. This relative excess creates a macroscopic magnetization. The macroscopic magnetization can also be described by a vector. This vector is defined as the summation of magnitudes of spin component vectors with same orientation. The macroscopic magnetization cannot be measured in its static state due to the overwhelming field strength of the external magnetic field. Only a precessing and phase coherent magnetization vector in a plane transverse to the external magnetic field can generate oscillating electric voltage according to Faraday's law of induction. This induced voltage is the NMR signal and can be measured through receiving coils at echo time (TE) (Brown et al., 2014).

To convert the non-measurable static longitudinal magnetization into measurable precessing and phase coherent transverse magnetization, RF pulses need to be applied. A RF pulse is an additional and temporary magnetic field, oscillating around the external magnetic field at the matching Larmor frequency. RF pulses transfer energy into the spin

system and flip the orientation of the magnetization vector in any desired direction from 0 to 180 degrees. The flip angle, classically amounting to 90 degrees, can be controlled with duration and amplitude of the RF pulse. The RF pulse can fully convert the static longitudinal magnetization vector into a precessing and phase coherent transverse magnetization vector. This conversion of magnetization is called spin excitation. After the RF pulse is switched off, the transverse magnetization decays to the benefit of the energetically more favorable longitudinal magnetization. Basically, the spin system is coming back to its thermal equilibrium defined by the external magnetic field. This process is known as spin relaxation or spin-lattice relaxation. Additionally, the magnetization vector is dismembering over time into the individual transverse spin component vectors, each of which precessing with a different phase due to spin-spin relaxation, a phenomenon also called dephasing. This is attributable to molecular mechanisms, fluctuating additional fields and spatial field strength inhomogeneities, which in the aggregate lead to marginal frequency differences of spin precession. The NMR signal intensity is at its maximum right after the RF pulse is switched off. At this very moment, the magnetization vector is phase coherent and rotating in a transverse plane in relation to the external magnetic field. Therefore, the magnetization vector magnitude is the greatest, which means that the biggest amount of voltage will be induced in receiving coils. Molecular mechanisms, fluctuating additional fields and spatial field strength inhomogeneities cause substantial loss of transverse magnetization and therefore signal intensity (Brix et al., 2008).

Recovery of longitudinal magnetization and decay of transverse magnetization can be described by exponential functions with associated time constants named T1 and T2. These time constants of spin relaxation are unique for different solids, fluids and biological tissues. They reflect, in a complex manner, the interaction of non-zero spins with their surroundings. T1 and T2 are characteristic parameters mainly generating the image contrast in MRI. Image contrast means to be able to differentiate signal intensities of two nearby but distinct structures (Brix et al., 2008; Bushong & Clarke, 2014).

Molecular mechanisms, fluctuating additional fields and spatial field strength inhomogeneities lead to T2* in biological tissues. T2* is much shorter compared to the theoretical transverse relaxation T2 of $_1$H hydrogen isotopes. Spatial field strength inhomogeneities are unique for each MR scanner and always lead to the same symmetric dephasing pattern of stationary spins, assumed the influence of fluctuating additional fields can be neglected. In this simplified model, each stationary spin is precessing with its own frequency, either clockwise or counter-clockwise after spin excitation due to spatial field strength inhomogeneities. The symmetric dephasing leads to a wider and wider spreading hand fan shaped figure of transverse spin component vectors. The magnetization vector is basically fanning out (Brix et al., 2008).

Spatial field strength inhomogeneities can be compensated with the spin echo sequence, which incorporates an additional 180 degrees RF pulse at ½ TE. The additional 180 degrees RF pulse simply mirrors the dephasing spins in the transverse plane but will not affect direction and speed of precession. Spins come together symmetrically until the hand fan of transverse component vectors has been closed again and spins are in phase exactly at TE. This will maximize the amount of induced voltage during signal sampling. The signal has been enhanced by the presence of the 180 degrees pulse at ½ TE. The rephasing at TE through an additional 180 degrees RF pulse is called spin echo. The magnetization vector magnitude at TE is now independent of spatial field strength inhomogeneities and the measured decay of transverse magnetization T2* is closer to the isotope specific T2. The spin echo sequence is therefore capable to extend the time where the NMR signal is detectable and will lead to a stronger NMR signal. Fluctuating fields cause irreversible dephasing which cannot be compensated. The additional RF pulse at ½ TE will unfortunately increase the time of signal acquisition, which can be a major drawback when speed is crucial to picture moving structures, for example. To accelerate signal acquisition, a simpler pulse sequence called gradient echo pulse sequence needs to be applied, where only one RF pulse is used for a short angle excitation of spins between 0 and 15 degrees, to speed up longitudinal magnetization recovery. Gradient echo sequences are used, although

signal loss from spatial field strength inhomogeneities will not be compensated (Brix et al., 2008).

To get spatial sensitivity, a general property needs to be utilized to distinguish between different positions within a scanned volume. As mentioned above, beside the gyromagnetic ratio, the Larmor frequency is depending on the local magnetic field strength. A linear variation of the Larmor frequency along three axes is imaginable, if the external magnetic field strength could be modulated along these axes. This can be achieved with small additional and temporary magnetic fields. These temporary magnetic fields create longitudinal, transverse and oblique magnetic field gradients within the external magnetic field. In MRI, temporary magnetic fields to create gradients within the external magnetic field are used for selective excitation of spins and spatial encoding of the NMR signal in a previously excited volume or slice (Brix et al., 2008; Bushong & Clarke, 2014).

Now spins can be excited only in a single slice of a sample along the direction of a gradient magnetic field where the Larmor frequency of spins agrees precisely with a chosen spectral range of the RF pulse. Such a gradient within the external magnetic field is called slice-selective gradient. The spectral range of the RF pulse defines the thickness of a slice along the slice-selective gradient. A slice-selective gradient and RF pulse must be applied simultaneously to excite spins (Brix et al., 2008; Brown et al., 2014).

The next step has to be the localization of the NMR signal inside the selected slice. To ensure this, another magnetic field needs to be switched on temporarily in orientation of one of the in-plane dimensions of the selected slice. This gradient is called frequency-encoding gradient. It is not switched on simultaneously with the RF pulse. Instead, it is switched on while the NMR signal is sampled at TE. The sampled signal is now consisting of many component signals, each of which with a different frequency and amplitude, if the scanned volume has an inhomogeneous proton density. All spins in a column perpendicular to the frequency-encoding gradient are exposed to the same field strength and precess with the same frequency. The frequency is different depending on location in relation to the magnetic field gradient. The derived

summation signal of oscillating current is a complex wave function. Its components can be extracted with the Fourier transformation (FT). After FT, signal amplitudes are arrayed in terms of frequency. The signal intensity pattern, which represents the proton composition of a sample, has now been spatially encoded along one dimension of the selected slice (Brix et al., 2008).

The induction signal can only be sampled during a restricted period of time, before it gets lost because of decay of transverse magnetization and loss of phase coherency after spin excitation. Further, length of sampling steps during TE cannot be reduced in an arbitrary way. This leads to a restricted amount of measured values that can be digitalized and subsequently analyzed with FT. The quantity of sampling steps during TE directly determines spatial resolution along the direction of the frequency-encoding gradient. To be more specific, the number of image voxels along the frequency-encoding gradient is identical with the number of sampling steps that are digitalized during TE. Consequently, spatial resolution along the frequency-encoding gradient is limited (Brix et al., 2008; Bushong & Clarke, 2014).

The second in-plane dimension will be encoded with multiple applications of additional and temporary magnetic fields, each of which with different field strengths in orientation of the second in-plane dimension. These gradients are called phase-encoding gradients. Phase-encoding gradients must be applied between the RF pulse and TE. The slopes of magnetic field gradients are rising with each repetition cycle, which starts with a RF pulse, due to increasing field strength of the phase-encoding gradients in equidistant steps. Once more, frequency of spin precession will change along with magnetic field gradients. This has a direct impact on the phase angle of spin precession. After a phase-encoding gradient has been switched off, component vectors of the transverse magnetization are precessing with the same frequency again but with a different phase angle according to their location in relation to the previously applied phase-encoding gradient. Thus, different phase angles are inherited in the sampled signal after the application of each phase-encoding gradient (Brix et al., 2008; Bushong & Clarke, 2014).

Different gradient slopes create a family of lines of magnetic field gradients intersecting in the so-called isocenter. The isocenter is a location within the external magnetic field where the field strength is always identical with the external magnetic field itself. Around the isocenter, magnetic field gradients are increasing and decreasing in linear fashion along the direction of applied gradients. However, the amount of phase change across a fixed distance, anywhere along a magnetic field gradient, will be the same since the slopes are linear. Therefore, a contrast needs to be drawn with multiple applications of different phase-encoding gradients. At the isocenter the value of gradient slopes is always zero. Hence, no phase change occurs at the isocenter. The further one moves away from the isocenter, phase change will increase because of increasing gradient slopes. Therefore, the last in-plane dimension is encoded in the amount of phase change of spins in relation to the isocenter. In other words, spatial information is imbedded in the comparison of phase change of spins caused by the different phase-encoding gradients. Another FT can now spatially decode the different amount of signal amplitude according to a location dependent change of phase (Brix et al., 2008).

The phase-encoding technique is more time consuming then the frequency-encoding technique. A frequency-encoding gradient must be applied only once while the phase-encoding gradient must be applied numerous times to get an acceptable spatial resolution. While the spatial resolution along the frequency-encoding gradient depends on the number of sampling steps during TE, spatial resolution along the phase-encoding gradient depends on the number of applications of phase-encoding gradients (Brix et al., 2008).

Varieties in frequency and phase are both direct correlates of NMR signal location in two different dimensions of a selected slice. The two encoding techniques combined form the basis of the 2D FT imaging method. Number of sampling steps during TE in the presence of the frequency-encoding gradient (N) and number of applications of the phase-encoding gradients (N) form a matrix of N × N data points. This 2D matrix of raw data arranged in columns (frequency domain) and rows (phase domain) is called k-space. The k-space can be transformed directly with 2D FT

into a MR image of a selected slice with a N × N pixel resolution. Depending on the pixel spacing, a wide or narrow anatomic region can be analyzed with the image or field of view, respectively (Brix et al., 2008).

4 Four-Dimensional Flow Cardiovascular Magnetic Resonance

Four-dimensional (4D) flow CMR provides information regarding velocity and direction of blood flow as well as signal intensity magnitude. This combined information is available for all three spatial dimensions, at several time points respectively time frames of the cardiac cycle and each voxel inside the acquired volume. With a single acquisition, it is possible to quantify blood flow (Gabbour et al., 2013; Jarvis et al., 2016; Nordmeyer et al., 2010) as well as to assess basic anatomic features, in a freely selectable region of interest (ROI) and at a reasonably high spatiotemporal resolution (Hanneman, Kino, Cheng, Alley, & Vasanawala, 2016).

4D flow CMR is using the principles of phase contrast (PC) imaging. PC imaging is based on the fact that moving spins accumulate a different phase shift than stationary spins in the presence of magnetic field gradients over time. Velocity is encoded by so-called velocity-encoding gradients. Phase shift induced by gradients is proportional to gradient application time and strength. A bipolar pair of gradients for example, with same strength and duration but opposite polarity, applied consecutively along the slice-selective dimension, will induce a net phase shift of zero degrees in stationary spins. At the same time, spins that are moving along the direction of the velocity-encoding gradient will have a non-zero phase shift because the gradient strength is incrementing and decrementing in relation to the isocenter. Thus, the faster spins are moving away or towards the isocenter, the bigger the difference of gradient strength will be between the two consecutive gradient applications and therefore the accumulation of phase shift. In summary, the measurable phase angle or phase shift for constantly moving spins along the direction of a bipolar pair of gradients is directly proportional to the velocity of spin movement (Carr & Purcell, 1954; Hahn, 1960).

To lower unwanted background phase offset susceptible to magnetic field inhomogeneities, which cannot be refocused by bipolar gradients, it is necessary to generate a flow-compensated reference data set with identical acquisition parameters but different velocity-encoding gradients,

compared to the flow-sensitive acquisition. After subtraction of the flow-compensated and flow-sensitive data sets, it is possible to calculate a 2D velocity map for a single time frame of the cardiac cycle by the derived PC and to generate a PC image. Information about signal intensity magnitudes is converted into corresponding magnitude images which will depict the patient's anatomy (Bryant, Payne, Firmin, & Longmore, 1984). The velocity-encoding gradient strength needs to be chosen carefully. If the gradient strength is set up too high, it will result in noise or random phase error in PC images. Therefore, an unnecessarily high velocity-encoding gradient strength will lead to a false determination of absolute velocities (Lotz, Meier, Leppert, & Galanski, 2002).

The velocity-encoding value (VENC) helps to set up the right gradient strength. The VENC defines the maximum velocity which is leading to a phase shift of ±180 degrees in the presence of a velocity-encoding gradient with a certain strength and duration. The sign of accumulated phase represents flow direction in relation to the velocity-encoding gradient (Lotz et al., 2002).

If velocities inside the acquired volume exceed the set up VENC, phase shift will suddenly change signs, which is equivalent to flow reversal inside of an otherwise spatially and temporally homogenous blood stream in reconstructed PC images. The misregistration of flow direction due to a falsely chosen VENC is called phase aliasing also referred to as velocity aliasing. Thus, if the velocity-encoding gradient strength is set up to low, maximum velocities will be measured inaccurately, too.

To address hemodynamic changes throughout the cardiac cycle, several frames need to be pictured, from the beginning of systole to the end of diastole, for a sequence of time-resolved images (CINE). Through-plane velocity-encoding over the cardiac cycle perpendicular to a vessel lumen is known as 2D CINE PC-MRI (Lotz et al., 2002).

Imaging techniques are still not fast enough to collect all necessary data to fill up the two k-spaces per frame for a 2D CINE PC image within one cardiac cycle. That is why the k-space needs to be divided. Only a part of all required in-plane phase-encoding steps are measured for each data set per frame and heartbeat, which is called k-space segmentation. The number of k-space lines collected for one data set per frame during one

cardiac cycle defines the value of the so-called k-space segmentation factor. Electrocardiogram (ECG) triggered phase-encoding steps are repeated over multiple cardiac cycles until all of k-space is complete. Thus, CINE images always represent averaged hemodynamic information of multiple heartbeats per frame. The time which is covered by a single frame or the temporal resolution, is determined by the following factors: value of the k-space segmentation factor multiplied by the time between two consecutive RF pulses or repetition time (TR) multiplied by number of data sets per frame (Markl, Frydrychowicz, Kozerke, Hope, & Wieben, 2012).

The standard two-point method can be extended to a four-point method. Instead of two data sets per frame, four will be acquired. One flow-compensated reference data set and one flow-sensitive data set for each spatial dimension (Pelc, Bernstein, Shimakawa, & Glover, 1991).

A 2D flow acquisition can be conducted in one breathhold, while a 4D flow acquisition takes much longer. Three-dimensional (3D) volume coverage makes it necessary to phase encode not only one in-plane dimensions but a second dimension in the slice-encoding direction. To memorize, scan time depends mainly on the number of phase-encoding steps. 4D flow scan time in heartbeats can be estimated by the following equation: number of phase-encoding steps along the slice-encoding direction multiplied by the number of in-plane phase-encoding steps divided by the value of the k-space segmentation factor (Markl et al., 2012).

Today, data acquisition is more efficient, which makes it possible to incorporate 4D flow assessments into clinical imaging protocols. The development of faster and stronger gradient systems, to the benefit of shorter TRs and TEs as well as multichannel coil receivers to enable parallel imaging (PI), has reduced scan time from the hardware perspective. The implementation of PI was a key factor to a substantial gain of speed in MR image acquisition. PI makes it possible to undersample k-space in phase-encoding directions to directly reduce the total number of phase-encoding steps (Deshmane, Gulani, Griswold, & Seiberlich, 2012).

Receiving coils at different positions in relation to the signal source detect distinct induced voltages and therefore contribute to the spatial encoding

of the NMR signal. This spatial receiver sensitivity can be used to generate various images from each receiver channel. Concomitant redundancy in spatial information can be used to undersample k-space by a factor that is dependent on the number of channels and coils as well as geometry of coil arrangement. For example, with the right hardware, either every second k-space line can be excluded from phase-encoding or the distance between two adjacent k-space lines can be doubled. In both cases scan time would be decreased twofold (Hamilton, Franson, & Seiberlich, 2017).

Missing k-space lines have to be recovered with methods like GRAPPA before reconstructed images from each receiver channel can be combined with a sum-of-squares algorithm to complete the image matrix (Griswold et al., 2002).

A different strategy to overcome image artifacts from undersampling is represented by the SENSE approach. K-spaces with an increased distance between sampling positions will be reconstructed first. The reduced sampling density causes a characteristic foldover aliasing in the image matrix due to a smaller field of view. Signal superimposition in each aliased voxel from the reduced field of view can be resolved according to the spatial receiver sensitivity weightage. Eventually, intermediate images can be put together to a final image that covers the full field of view without foldover aliasing (Pruessmann, Weiger, Scheidegger, & Boesiger, 1999). Spatial sensitivity information from SENSE can be transferred to k-t SENSE. First, a set of low-resolution training frames is acquired where only the center of k-space is covered by phase-encoding steps. In the acquisition stage, k-space lines in phase-encoding directions are undersampled by a factor of x in a slightly asymmetric fashion. Missing k-space can then be recovered by using the training data in combination with spatial receiver sensitivities, to exploit signal correlations in k-space and in time (Tsao, Boesiger, & Pruessmann, 2003). The same idea of correlation between k-space at different time points can be transferred to GRAPPA. The k-t GRAPPA method uses also data from adjacent time frames to exploit spatiotemporal correlations to recover k-space from phase-encoding undersampling (Huang, Akao, Vijayakumar, Duensing, & Limkeman, 2005).

Another concept to reduce scan time is named compressed sensing. Compressed sensing is derived from literature about information theory as well as approximation theory and was developed based on an abstract general background to become an applied tool to recover randomly undersampled k-space (Lustig, Donoho, & Pauly, 2007).

Johnson and colleagues introduced non-Cartesian signal sampling in the form of radial trajectory sampling schemes to accelerate acquisitions by undersampling phase-encoding steps (K. M. Johnson et al., 2008)

More recently, Sigfridsson and colleagues have introduced spiral signal sampling in contrast to Cartesian k-space acquisition. It has been shown that TR-interleaved spiral readout trajectories reduce scan time two-fold compared to the regular Cartesian k-space sampling pattern (Sigfridsson, Petersson, Carlhall, & Ebbers, 2012).

Dyvorne et al. were able to combine spiral sampling with compressed sensing reconstruction successfully to accelerate 4D flow acquisition up to a breathhold (Dyvorne et al., 2015).

Besides all improvements of the various approaches regarding the time penalty, free breathing during 4D flow CMR acquisition is still inevitable. Therefore, motion artifacts from breathing need to be compensated to reduce image quality impairment and degradation of flow quantification (Dyverfeldt & Ebbers, 2017).

One-dimensional respiratory navigator gating is the most common technique to do so in 4D flow CMR (Markl et al., 2007). Drawbacks include hysteresis of the lung through the breathing cycle, indirect estimation of respiratory heart movement from respiratory diaphragm movement, neglect of movement other than in the craniocaudal direction, interpatient variability of respiratory heart movement, interruption of acquisition, decrease of temporal resolution and a more complex scan planning. A navigator can track the right hemidiaphragm in the craniocaudal direction at the end of diastole using an additional spin echo sequence with oblique alignment of the RF pulse and the 180 degrees refocusing pulse. The navigator field of view is defined as the overlapping area of the two. A 2D pulse sequence with signal sampling orthogonal in relation to the RF pulse can be implemented instead (Firmin & Keegan, 2001).

Acquired k-space segments are only accepted when the lung-liver interface is within a tolerance range of ±3 mm compared to a reference acquisition where the diaphragm has been located, at the end of a breathing cycle or the most akinetic respiratory phase, for example. Otherwise, k-space segments will be rejected and the trigger to advance data acquisition to the next segment is withhold (Wang et al., 1996). Thus, study time is also dependent on the navigator acceptance rating or the patients breathing rhythm, frequency and amplitude. Pressure-sensing bellows can be used as an alternative to internal respiratory motion surrogates for motion compensation (Markl, Chan, et al., 2003; Santelli et al., 2011). Further attempts to improve respiratory motion compensation include self-navigator methods (Uribe et al., 2009), among others (Akcakaya et al., 2014; van Ooij et al., 2015).

After data acquisition has been completed, certain sources of error need to be corrected before flow quantification and visualization can be performed more unambiguously. Sources of error mainly include concomitant field gradient effects specified by the Maxwell terms (Bernstein et al., 1998), non-linear field gradients (Markl, Bammer, et al., 2003), eddy currents (Walker et al., 1993) and velocity aliasing (Loecher, Schrauben, Johnson, & Wieben, 2016; Xiang, 1995). These effects, barring velocity aliasing, alter the phase signal by background phase offset through induced currents or spatiotemporal inhomogeneities of magnetic field gradients, which could not be eliminated through phase image subtraction or phase refocusing of stationary tissue with bipolar gradients. This is important to note, especially in 4D flow CMR studies, since volume coverage is big and inhomogeneities of magnetic field gradients increase in a non-linear fashion the further one moves away from the isocenter (Lorenz et al., 2014).

The process of error correction involves automated methods during image reconstruction as well as data processing and additionally user supported methods during data processing. Different sources of error can be addressed with different kinds of correction methods. Consequently, various possible combinations have been applied to overcome phase offset as well as phase aliasing and no standardized approach has

become apparent since Dyverfeldt et al. published their consensus statement on 4D flow CMR (Dyverfeldt et al., 2015).

When data is corrected, blood flow can be visualized by vector fields, pathlines, streamlines, intensity projections and the like as well as quantified in cardiac chambers and great vessels (Markl et al., 2016).

5 Pressure Gradients

Blood needs energy to flow through arteries, capillaries, veins and cardiac chambers. This mechanical energy is provided by the heart and can be decomposed into static and kinetic energy. According to the law of conservation of energy, static and kinetic energy can be freely interconverted without energy loss inside a closed system. For example, during systole the myocardial contraction generates static energy in form of pressure. With the opening of the semilunar valves, pressure is converted into kinetic energy or velocity without a loss of energy and blood begins to flow through the cardiovascular system (Akins, Travis, & Yoganathan, 2008).

Due to friction, kinetic energy is transformed into acoustic noise and for the most part into heat. Heat cannot be retransformed into kinetic or static energy and is therefore said to be lost to further drive the blood flow. For example, blood viscosity creates friction between blood components with different velocities, especially at the vessel boundaries. This loss of kinetic energy into heat due to viscous dissipation inside the cardiovascular system is unavoidable, even for laminar blood flow (Akins et al., 2008).

To sustain the blood flow across a segment of the cardiovascular system with a decreased diameter, such as a stenotic valve, blood velocity must increase to compensate for the smaller cross section. This physiologic principle is characterized by the Gorlin formula (Gorlin & Gorlin, 1951).

When the total energy inside the stenotic valve is assumed to be conserved, then pressure within the obstructive lesion must decrease in proportion to the velocity increase. This decrease in pressure in proportion to the increase in velocity creates a maximum pressure gradient between the ventricle and the stenotic valve. With a normalized vessel diameter in the poststenotic area, velocity is returning to the prestenotic level to conserve blood flow and likewise pressure is recovering. However, because some additional kinetic energy has been lost across the obstructive lesion, pressure is not recovering to the full prestenotic potential and a pressure gradient remains. Because of pressure recovery in the poststenotic area, transvalvular pressure gradients will be smaller compared to the maximum pressure gradient at

the level of the most narrow lumen cross-section of a stenotic valve (Akins et al., 2008).

When the bloodstream enters a wider poststenotic vessel segment such as a dilated aorta and/or the valve orifice gets smaller over time, turbulent flow is likely to occur. Onset of turbulent flow in the cardiovascular system can be predicted when the Reynolds number exceeds a certain threshold. The Reynolds number is determined by the quotient of blood velocity, vessel diameter and blood density divided by blood viscosity. Turbulent blood flow can be described as random spatiotemporal differences of blood velocities and blood flow directions causing friction (Schlichting & Gersten, 2017).

In the presence of non-laminar flow, a significant amount of kinetic energy is converted into heat and is no longer available for pressure recovery. Turbulent flow is the main reason for a loss of kinetic energy due to obstructive lesions, beside other pathological non-turbulent flow formations. Hence, the measurable transvalvular pressure gradient will be greater in obstructive lesions causing turbulent flow compared to lesions with more regular flow patterns (Akins et al., 2008).

The energy loss across an obstructive lesion must be compensated by an increased workload of the heart, to maintain blood flow at a reasonable level. To do so, the heart must raise the intraventricular pressure during systole and/or the cardiac output. An excessive workload for a longer period of time may result in irreversible damage of the myocardium and a subsequent inability to generate enough energy to sufficiently drive the blood flow (Travers, Kamal, Robbins, Yutzey, & Blaxall, 2016).

If the insufficient heart is too weak to overcome a severe stenosis, no pathologically increased velocities or pressure gradients can be seen across the lesion in patients with chronic heart failure of higher grades. The additional cardiac workload or myocardial stress is proportional to the additional energy loss due to any kind of friction caused by obstructive lesions. Therefore, additional cardiac workload can be estimated with the transvalvular pressure gradient, given that the function of the heart is still preserved in general. Hence, the true pressure gradient across a stenosis is a direct measure for the hemodynamic significance of obstructive lesions (Akins et al., 2008).

Blood pressure gradients also known as pressure drops, pressure losses or pressure differences serve to grade severity of obstructive valvular conditions, together with a medley of other pathophysiological determinants, respectively biomarkers (Baumgartner et al., 2010; Nishimura et al., 2014).

To justify an invasive therapy with the intention to favor the course of affected patients, different criteria must be fulfilled like the presence of physical complaints and/or a certain grade of disease severity. According to this, measuring biomarkers correctly and at best without causing harm is crucial for the right care of patients (Eicken et al., 2011; Vahanian et al., 2012).

Cardiac catheterization is the genuine gold standard method to quantify absolute pressure gradients in the cardiovascular system. The catheter tip is moved towards the ROI under fluoroscopic guidance. Dynamic, periodic and complex blood pressure waveforms, generated by one of the four cardiac chambers, will be directly transmitted via the irrigation solution inside the hollow catheter wire to a deflectable membrane, respectively pressure transducer, which is electromechanically coupled with a recording device and synchronized with an ECG. The measurement may be repeated another time, proximal or distal in relation to the first measuring point, to be able to calculate a non-synchronous peak-to-peak systolic gradient between the two points. Two distant catheters, applied at the same time, can be used to synchronize measurements for the calculation of instantaneous and mean pressure gradients over the cardiac cycle (*Cardiovascular Catheterization and Intervention: A Textbook of Coronary, Peripheral, and Structural Heart Disease*, 2010).

In the echocardiographic laboratory, peak instantaneous pressure gradients inside obstructive lesions are estimated mostly using the simplified Bernoulli equation with maximum velocities, measured by the Doppler principle in vessels and cavities close to the body surface (Currie, Seward, Fyfe, Bove, & Taji, 1986). Moreover, it is possible to acquire the necessary information about velocities with 2D CINE PC images perpendicular to the vena contracta (Kilner et al., 1993).

Alternatively, it is possible to calculate relative pressure gradients with the simplified Gorlin formula. In this approach only anatomic CMR images of patients with obstructive valvular conditions are used to measure the cardiac output and valve orifice area to finally estimate the transvalvular pressure gradient (Valenti et al., 2015).

A specialized field of fluid mechanics, called computational fluid dynamics (CFD), uses patient specific information about anatomy and physiology from different kinds of imaging modalities such as CT angiography or PC MRI, to produce flow and pressure fields from complex computer simulations to ultimately estimate pressure gradients among other biomarkers (Coogan, Humphrey, & Figueroa, 2013; Goubergrits et al., 2015; Mirzaee et al., 2017).

Dyverfeldt and colleagues used 4D flow CMR data to characterize turbulent kinetic energy in the ascending aorta of patients with aortic stenoses and estimated pressure losses by the volumetric integration of turbulent kinetic energy, mapped distal to obstructive lesions (Dyverfeldt, Hope, Tseng, & Saloner, 2013).

Lately, Donati et al. evaluated the work-energy principle for relative pressure gradient estimation by 4D flow CMR (Donati, Figueroa, Smith, Lamata, & Nordsletten, 2015).

Furthermore, a relative pressure field inside a user-defined and time-averaged ROI of the cardiovascular system can be calculated from a velocity field, generated by 4D flow CMR, based on the Navier-Stokes equations (NSE) for incompressible fluids with laminar flow conditions. Along a centerline, which connects midpoints of adjacent lumen cross sections, the relative pressure field can be integrated into peak instantaneous pressure gradients between two points by solving the Pressure Poisson equation (PPE) (Bock et al., 2011; Ebbers & Farneback, 2009; Ebbers, Wigström, Bolger, Engvall, & Karlsson, 2001; Krittian et al., 2012; Meier et al., 2013; Riesenkampff et al., 2014; Tyszka, Laidlaw, Asa, & Silverman, 2000; Yang, Kilner, Wood, Underwood, & Firmin, 1996).

6 Aim of the Study

The first clinical study which evaluated agreement between relative pressure gradient measurements by cardiac catherization and four-dimensional flow cardiovascular magnetic resonance, using the Navier-Stokes and Pressure Poisson equations, was focused on mild to moderate stenotic lesions of the aorta as part of the high-pressure circuit of the cardiovascular system (Riesenkampff et al., 2014).

The aim of this study is to further investigate the agreement between invasive catheter measurements and this non-invasive diagnostic approach. Therefore, this non-invasive diagnostic approach was applied in patients with stenotic and/or insufficient lesions of the right ventricle outflow tract as part of the low-pressure circuit of the cardiovascular system. Right ventricle outflow tract pathologies were either congenital or secondary to congenital heart disease. Agreement was estimated retrospectively, between peak-to-peak systolic gradients measured by cardiac catheterization and peak instantaneous pressure gradients measured by four-dimensional flow cardiovascular magnetic resonance, using the Navier-Stokes and Pressure Poisson equations.

7 Methods

The population of this study was recruited by the Klinik für Kinderkardiologie und Angeborene Herzfehler, Deutsches Herzzentrum München des Freistaates Bayern, Klinik an der Technischen Universität München, Germany. The data were analyzed retrospectively.

Patients included into the study population had to fulfill inclusion criteria shown in table 1 and were disqualified for exclusion criteria displayed in table 2.

Table 1. Inclusion criteria.

Congenital right ventricle outflow tract pathology (regurgitation and/or stenosis)
Right ventricle outflow tract pathology secondary to congenital heart disease (regurgitation and/or stenosis)
Time difference between procedures ≤ 1 day

Table 2. Exclusion criteria.

Remaining phase aliasing after correction in phase contrast images
Magnetic resonance artifacts in magnitude images
Time difference between procedures > 1 day

Prior to routine cardiac catheterization and CMR procedures, all patients or their legal guardians had given a written consent.

A standard CMR examination starts with a simple localizer sequence to assess the individual anatomy broadly. Based on localizer images, common 2D CINE PC images acquired in free breathing are planned perpendicular to the vessel cross sections of the main pulmonary artery (MPA), left pulmonary artery (LPA) and right pulmonary artery (RPA) as well as the aorta, as part of most routine CMR protocols tailored for patients with CHD. 2D CINE PC images are used to estimate the required VENC in case of a following 4D flow measurement. 2D CINE PC images are obtained as previously described (Chai & Mohiaddin, 2005; Fratz et al., 2013).

Images are checked during the examinations for possible velocity aliasing. In case of flow misregistration, involved data is rejected and the VENC is set to a higher value before the affected acquisition is redone. The process will be repeated until no more aliasing occurs. The highest VENC of the final 2D CINE PC acquisitions, which has been geared towards the ROI, can then be used for the following 4D flow acquisition.

A RF spoiled gradient echo pulse sequence with small angle excitation was applied for 4D flow acquisitions with focus on the RV, RVOT and MPA as well as the LPA and RPA, in patients for whom either a therapeutic and/or diagnostic cardiac catheterization had already been scheduled, or was highly likely to be scheduled, because of congenital RVOT pathologies or RVOT pathologies secondary to CHD.

Again, localizer images were used to position the 3D volume edges correctly according to the given anatomy. The scan volume was phase encoded in craniocaudal or dextrosinistral direction. The in-plane phase-encoding gradient was set in the dorsoventral direction. Prospective ECG-gating was used to synchronize the acquisition trigger with the cardiac cycle. The right hemidiaphragm was tracked in the craniocaudal direction, with a crossed pair of spin echo sequences at the beginning of each cardiac cycle, to compensate respiratory motion by navigator gating. The user-defined reduction factor, with the purpose to decrease the number of phase-encoding steps, was set to the value 5. Missing k-space was recovered with the PEAK-GRAPPA method (Jung et al., 2008). For

some patients, gadolinium-based contrast agent was used during the regular CMR protocol prior to the 4D flow sequences, to unmask potential ischemic myocardial lesions, for example. No sedation was used during CMR scans. 4D flow CMR data was generated as follows (Markl et al., 2007; Markl, Kilner, & Ebbers, 2011) and more detailed acquisition characteristics of included patients are given in table 3.

Table 3. Scan parameter.

	Median	Range
Spatial resolution [mm^3]	2.5 × 2.34 × 2.34	2.1 - 2.5 × 1.8 - 2.5 × 1.8 - 2.5
K-space segmentation factor	2	-
Temporal resolution [ms]	38.4	36.9 - 40
Partial k-space coverage [pct.]	83	69.4 - 83
Flip-angle [deg.]	7	7 - 10
Velocity encoded gradient [m/s]	3.5	2 - 5
Slices	40	24 - 48
Slab [mm]	87.2	58.5 - 120
Bandwidth per pixel [1/s]	445	445 - 490
Scan time [min]	9.36	5.1 - 19.5
Echo time [ms]	2.3	2.3 - 2.5
Repetition time [ms]	4.8	4.6 - 4.9
Field of view [mm^2]	240 × 300	225 - 340 × 240 - 349
Frames	19	12 - 24
Navigator window [mm]	±3	-
Navigator acceptance rate [pct.]	45	30 - 80

CMR procedures were performed with a whole-body, 1.5 Tesla, Magnetom® Avanto scanner, provided by Siemens Healthcare in Erlangen, Germany.

4D flow CMR data sets, consisting of one magnitude data set and three phase contrast data sets for each axis of the coordinate system, were reconstructed automatically after acquisition with the scanner related software Syngo version VB 18 and VD 13, provided by Siemens Healthcare in Erlangen, Germany. Image reconstruction included a correction of concomitant field gradients.

The DICOM files were then transferred with a portable storage medium from the in-house picture archiving and communication system (PACS) to a personal computer for further data processing.

Before the blood flow could be analyzed more unambiguously, data sets had been corrected for potential phase aliasing and remaining background phase offset, resulting from inevitable eddy currents, gradient non-linearity as well as noise. To do so, the 4D flow analysis software MEVIS Flow version 10.0 was used, provided by the Fraunhofer Institute for Medical Image Computing in Bremen, Germany.

First, the remaining background phase offset was corrected semiautomatically. Therefore, stationary regions in magnitude images were visually identified over the cardiac cycle and across the volume. Stationary regions can be defined as a group of voxels with a degree of velocity fluctuation over time undercutting a certain threshold. The user-defined threshold is dimensioned with the standard deviation (SD) of velocity fluctuation within a voxel over the cardiac cycle.

Blood flow causes a velocity fluctuation with a mean SD and pulsatile character. On the other hand, noisy regions such as regions containing air have a velocity fluctuation with a high SD, while static regions have a velocity fluctuation with a low SD. The threshold value was set at the lowest percentile. Therefore, at least parts of the patient's dorsal thorax wall were included. Because in this setting included voxels are considered stationary, averaged velocity fluctuations over the cardiac cycle in these voxels can only arise from remaining background phase offset. According to this, a surface was fitted by polynomial approximation of higher orders through each stationary voxel for every frame and velocity encoded

direction, respectively. In the last step, the surface was subtracted from the corresponding PC image. Therefore, phase offset was corrected. Based on the above-mentioned assumptions noise was masked and thus reduced, too (Lankhaar et al., 2005; Walker et al., 1993).

Second, regions with present phase aliasing were corrected automatically over the cardiac cycle and across the volume. Phase aliasing can be described as a sudden spatial and/or temporal change of the velocity field, which is a violation of basic principles in physics. Since phase angles between 0 and ±180 degrees are illustrated in gray scale, aliasing occurs as a sharp shift from white to black or vice versa. Aliased regions were corrected by a region-merging algorithm up to a point all interfaces were smoothed (Jenkinson, 2003).

In the following step, corrected data was exploited to automatically calculate a time-averaged 3D PC MR angiogram (PC MRA). The calculation is based on information about absolute velocities in combination with signal magnitude weighting, to better distinguish between cardiovascular compartments and other anatomic structures (Bock et al., 2010). The individual PC MRAs were used to segment the acquired volume. Major parts of the ROI were labeled with inclusion seed points, while regions of no interest (e.g. ascending aorta) were labeled with exclusion seed points. A watershed algorithm was employed to flood the area around the inclusion seed points to create a 3D model of the RV, RVOT, and MPA as well as both pulmonary arteries. Areas, which were falsely covered by the algorithm, had to be corrected manually based on the given anatomy in magnitude images. Each 4D flow data set was segmented three times in total by one observer.

Thereafter, a relative pressure field was computed by the Navier-Stokes equations for each of the three segmented 3D models per patient on grounds of the determined flow information, after the divergent part of the velocity field was removed, based on a finite element approach.

Blood density and blood viscosity, two variables of the Navier-Stokes equations, were set to the same standard values in each case of calculation as follows:

$$1.06 \times 10^3 \text{ kg/m}^3 \text{ and } 3.2 \times 10^{-3} \text{ Pa} \times \text{s}$$

The gravity force term was neglected. Per patient, one peak instantaneous pressure gradient between the RV and LPA as well as one peak instantaneous pressure gradient between the RV and RPA were computed along the respective centerlines for each of the three 3D models. Three peak instantaneous pressure gradients between the RV and LPA as well as three peak instantaneous pressure gradients between the RV and RPA were then averaged. The Pressure Poisson equation for peak instantaneous pressure gradient estimation was solved based on a finite element approach, too (Meier et al., 2013).

Chapter 7 summarizes the technical equipment involved in the process of 4D flow CMR data acquisition and data processing.

Routine cardiac catheterization procedures were done in the normal manner under sedation with oxygenation or artificial respiration in case of need. Blood pressure curves were obtained at points proximal and distal of present lesions, beside other measurement points in the pulmonary arterial flow area, at the discretion of the operating senior staff physician. Only single catheter techniques were used during procedures. No dual catheter techniques were used to measure simultaneous pressure curves at two different locations.

The recorded hemodynamic information and angiographic movies of performed procedures are stored in the form of CD-ROMs in the institutional catheter laboratory archive. CD-ROM printouts were used to manually size peak systolic pressure values from pressure curves for each measurement point. Depending on the patient's heart rate, one measurement point printout displays 3 to 7 peak systolic pressure values, as exemplified in figure 1. Therefore, sized peak systolic pressure values were averaged.

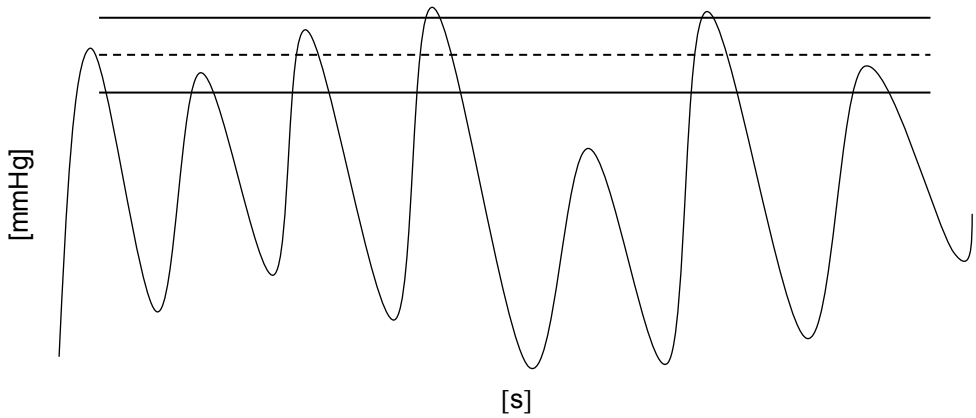

Figure 1. Fictitious pressure curve of a measurement point printout with mean peak systolic pressure value (dashed line) and standard deviation of peak systolic pressure values (solid lines).

Finally, one peak-to-peak systolic gradient between the RV and LPA as well as one peak-to-peak systolic gradient between the RV and RPA were calculated for each patient as follows:

$$\mathrm{RV}_{\text{mean peak systolic pressure value}} - \mathrm{LPA}_{\text{mean peak systolic pressure value}}$$

$$\mathrm{RV}_{\text{mean peak systolic pressure value}} - \mathrm{RPA}_{\text{mean peak systolic pressure value}}$$

More detailed information regarding the technical equipment and pharmaceuticals involved in cardiac catheterization procedures is given in chapter 7.

8 Materials

8.1 Technical Equipment

Table 4. Hardware.

Item	
Scanner	whole-body, 1.5 Tesla, MAGNETOM® Avanto, Siemens Healthcare, Erlangen, Germany
Coil	12-channel thorax coil, posterior and anterior each with a 2 × 3 array
Personal computer	Intel® Core i7-4790K 3.6 giga Hz, 16 GB RAM, NVIDIA GeForce GT 630 graphics card
Fluoroscopy	Artis zee, Siemens Healthcare, Erlangen, Germany
Catheters	4-6 French Berman/wedge/pigtail/others
Pressure transducer	Xtrans®, CODAN Medizinische Geräte GmbH & Co KG, Lensahn, Germany

Table 5. Software.

Item	
Scanner	Syngo, version VB 18 and VD 13, Siemens Healthcare, Erlangen, Germany
Hemodynamic analysis	AXIOM Sensis XP, version VC 11D, Siemens Healthcare, Erlangen, Germany
Personal computer	Windows® 7, Microsoft Corporation, Redmond, United States
4D flow analysis	MEVIS Flow, version 10.0, Fraunhofer Institute for Medical Image Computing, Bremen, Germany
Statistical analysis	SPSS Statistics, version 22, IBM Corporation, Armonk, United States Excel, version 16.0, Microsoft Corporation, Redmond, United States

8.2 Pharmaceuticals

Table 6. Pharmaceuticals used during cardiac catheterization procedures.

	Dosage	Use	Administration
Midazolam [mg]	3.75 - 9	obligate	oral
Propofol [mg/kg BW/h]	2 - 5	obligate	intravenous
Piritramide [mg/kg BW] / Fentanyl [µg/kg BW]	0.1 / 2 - 3	facultative	intravenous
Clonidine [µg]	15 - 30	facultative	intravenous
Atropine [mg]	0.1 - 0,25	facultative	intravenous
Ringer-Lactate [ml]	100 - 500	obligate	intravenous
Iodinated contrast agent [ml]	40 - 280	obligate	intravenous
Mepivacaine [mg]	10 - 30	obligate	subcutaneous

Table 7. Pharmaceuticals used during cardiovascular magnetic resonance procedures.

	Dosage	Use	Administration
Gadolinium-based contrast agent [mmol/kg BW]	0.15	facultative	intravenous
Saline [ml]	100 - 250	facultative	intravenous

9 Results

9.1 Study Population

3 female and 7 male patients (n=10) were included into the study population for retrospective analysis. Included patients were investigated between mid-2014 and mid-2015 as well as in spring of 2017. Reasons why patients were not included are listed in table 8. All cardiac catheterization and CMR procedures were performed at the German Heart Center Munich.

Table 8. Reasons why patients were not included.

Exclusion criteria	Number of patients
Remaining phase aliasing after correction in phase contrast images	6
Magnetic resonance artifacts in magnitude images	4
Time difference between procedures > 1 day	4

All included patients underwent a cardiac catheterization procedure because of stenotic and/or insufficient pulmonary valves or homografts and present a broad spectrum of CHD diagnoses, as listed in table 10. Scans of included patients were performed without sedation. A single patient received gadolinium-based contrast agent during a CMR procedure prior to the 4D flow sequence application because of a medical history including an acute episode of cardiac ischemia. The median spatiotemporal resolution of 4D flow CMR acquisitions was 2.5 × 2.34 × 2.34 mm^3 (2.1 to 2.5 × 1.8 to 2.5 × 1.8 to 2.5) and 38.4 ms (36.9 to 40). The median peak-to-peak systolic gradient was 26 mmHg with a 6.5 to 45 mmHg range. The median regurgitation in main pulmonary arteries or homografts was 22% with a 0 to 62% range. The median shunt ratio, quantified by the pulmonary to systemic flow volume rate ratio Qp:Qs, was 1:1 with a 0.7 to 1.2:1 range. The median time difference between procedures was 1 day with a 0 to 1 day range. The median radiation dose was 5170.2 $cGycm^2$ with a 132 to 35321.6 $cGycm^2$ range. The median

administration of iodinated contrast agent was 115 ml with a 40 to 280 ml range.

Patient characteristics and medical records of included patients can be extracted from table 9 and 10.

Table 9. Patient characteristics.

	Median	Range
Age [years]	23.7	6 - 62
Size [cm]	168	107 - 184
Weight [kg]	72	17 - 98
Body mass index[1] [kg/m2]	24	22.6 - 30.9
Body surface area[2] [m2]	1.82	0.7 - 2.6
Peak-to-peak systolic gradient [mmHg]	26	6.5 - 45
Main pulmonary artery or homograft regurgitation [pct.]	22	0 - 62
Shunt ratio [Qp:Qs]	1:1	0.7 - 1.2:1
Time difference between procedures [days]	1	0 - 1

[1] (WHO, 1995; WHO, 2000) [2] (Mosteller, 1987)

Table 10. Medical records.

Patient	Principal diagnosis	Correction procedure	Cardiac catheterization report	Invasive treatment	Cardiovascular magnetic resonance report
1	Tetralogy of Fallot (TOF)	Transannular patch plasty	Regurgitation III° / no shunt	Non	Regurgitation: main pulmonary artery (MPA) 63% left pulmonary artery (LPA) 65% right pulmonary artery (RPA) 46% / shunt ratio (Qp:Qs): 0.9:1
2	TOF	Transannular patch plasty	Regurgitation III° / no shunt / gradient: right ventricle (RV)-MPA 10 mmHg; MPA-LPA 10 mmHg	Dilatation	Regurgitation: MPA 41% LPA 38% RPA 21% / Qp:Qs: 0.8:1
3	Double outlet right ventricle (DORV) / ventricular septal defect (VSD) / pulmonary stenosis / transposition of the great arteries (TGA)	Rastelli procedure	No regurgitation / no shunt / gradient: RV-MPA 53 mmHg / small VSD	Non	No regurgitation / Qp:Qs: 1.1:1
4	TOF / right aortic arch / hypoplastic pulmonary valve	Transvalvular patch plasty	Regurgitation III° / gradient: MPA-LPA 17 mmHg	Non	Regurgitation: MPA 41% LPA 30% RPA 54% / Qp:Qs: 1.2:1
5	Persistent truncus arteriosus	patch / homograft plasty	No regurgitation / no shunt / gradient: RV-MPA 20 mmHg	Dilatation	Regurgitation: MPA 24% LPA 37% RPA 2%/ Qp:Qs: 1:1
6	Aortic valve regurgitation	Ross procedure	Regurgitation III° / gradient: RV-MPA 15 mmHg	Valve replacement	Regurgitation: MPA 45% LPA 38% RPA 25% / Qp:Qs: 1:1
7	Bicuspid aortic valve	Ross procedure	Regurgitation III° / gradient: RV-MPA 25 mmHg; MPA-RPA 12 mmHg	Valve replacement	Regurgitation: MPA 17% LPA 43% RPA 0% / Qp:Qs: 1.1:1
8	Aortic valve stenosis	Ross procedure	No regurgitation / gradient: RV-MPA 40 mmHg	Valve replacement	Regurgitation: MPA 5% LPA 13% RPA 0% / Qp:Qs: 1:1
9	Pulmonary atresia / VSD / patent ductus arteriosus (PDA) / hypoplastic pulmonary artery	Homograft plasty / VSD and PDA closure / LPA enlargement	Regurgitation / RV-MPA gradient not quantified	Dilatation	Regurgitation: MPA 22% LPA 11% RPA 16% / Qp:Qs: 1:1
10	DORV / VSD / pulmonary stenosis	Right ventricle outflow tract patch plasty / VSD closure / commissurotomy	Regurgitation / gradient: RV-MPA 20 mmHg	Dilatation	Regurgitation: MPA 19% LPA 15% RPA 29% / Qp:Qs: 0.7:1

9.2 Cardiac Catheterization and Four-Dimensional Flow Cardiovascular Magnetic Resonance Measurements

Table 11 compares the pressure gradients across the right ventricular outflow tracts measured invasively and derived from 4D flow CMR for each included patient, respectively.

One peak-to-peak systolic gradient contains hemodynamic information about two measurement point printouts. One printout for the RV and one printout for the RPA or LPA, respectively. However, depending on the heart rate, one printout contains hemodynamic information about 3 to 7 peak systolic pressure values, as exemplified in figure 1. Therefore, peak systolic pressure values were averaged.

The averaged coefficient of variation for the 30 mean peak systolic pressure values was 9% with a 1 to 29% range. Each coefficient of variation was calculated as follows:

$$\mathrm{SD}_{\text{of mean peak systolic pressure value}} \,/\, \mathrm{mean}_{\text{of peak systolic pressure values}}$$

The coefficient of variation is a simple relative measure of variance that puts the standard deviation in relation to the associated mean. A variance of 9% for all peak systolic pressure values is most likely attributable to a changing RV stroke volume, due to intrathoracic pressure changes over the respiratory cycle (Ruskin, Bache, Rembert, & Greenfield, 1973).

One mean peak instantaneous pressure gradient value contains hemodynamic information about three segmented volumes of one data set. However, one data set contains hemodynamic information about 5.1 to 19.5 minutes. The averaged coefficient of repeatability for the 20 mean peak instantaneous pressure gradient values was 4.9 mmHg with a 0 to 10.5 mmHg range. Each coefficient of repeatability was calculated as follows:

$$1.96 \times \mathrm{SD}_{\text{within-subject}} \times \sqrt{2}$$

The coefficient of repeatability defines a range in relation to the mean of differences. The difference between two independent measurements by the same method will lie within this defined range for 95% of investigated

subjects. Simply put, the difference between two peak instantaneous pressure gradient values computed based on two different segmentations will not exceed 4.9 mmHg in 95% of observations (Bland & Altman, 1999). 4.9 mmHg accounts for 19.7% of 24.9 mmHg, which is the mean of all peak instantaneous pressure gradients in this study population.

Since measurement points were probed just once in the catheter laboratory, only one peak-to-peak systolic gradient between the RV and LPA as well as one peak-to-peak systolic gradient between the RV and RPA could be calculated per patient. On the contrary, three peak instantaneous pressure gradients between the RV and LPA as well as three peak instantaneous pressure gradients between the RV and RPA could be generated with the 4D flow analysis software per patient. Therefore, comparison of repeatability of each method can only be evaluated to a limited degree. Nonetheless, the coefficient of repeatability for manual relative pressure gradient estimation with the 4D flow analysis software is 4.9 mmHg. Peak systolic pressure values vary with 9% on average over a span of several heartbeats.

Table 11. Results.

Patient	Gradient	peak-to-peak systolic gradient [mmHg]	mean peak instantaneous pressure gradient [mmHg]	Difference [mmHg]
1	RV-RPA	6.5	22.3	-15.9
	RV-LPA	9.5	12.0	-2.5
2	RV-RPA	8.8	11.7	-2.9
	RV-LPA	18.8	11.0	7.8
3	RV-RPA	34.7	43.7	-9.0
	RV-LPA	40.3	43.7	-3.3
4	RV-RPA	9.7	11.0	-1.3
	RV-LPA	25.8	22.0	3.8
5	RV-RPA	30.3	34.7	-4.3
	RV-LPA	28.3	33.7	-5.3
6	RV-RPA	14.3	17.3	-3.1
	RV-LPA	12.1	17.3	-5.3
7	RV-RPA	36.2	26.7	9.5
	RV-LPA	25.6	26.7	-1.1
8	RV-RPA	45.0	28.3	16.7
	RV-LPA	37.2	28.0	9.2
9	RV-RPA	36.0	36.0	0.0
	RV-LPA	32.0	30.7	1.3
10	RV-RPA	20.0	19.0	1.0
	RV-LPA	25.0	22.3	2.7
Mean		24.8	24.9	-0.1
SD		11.8	10.2	7.2

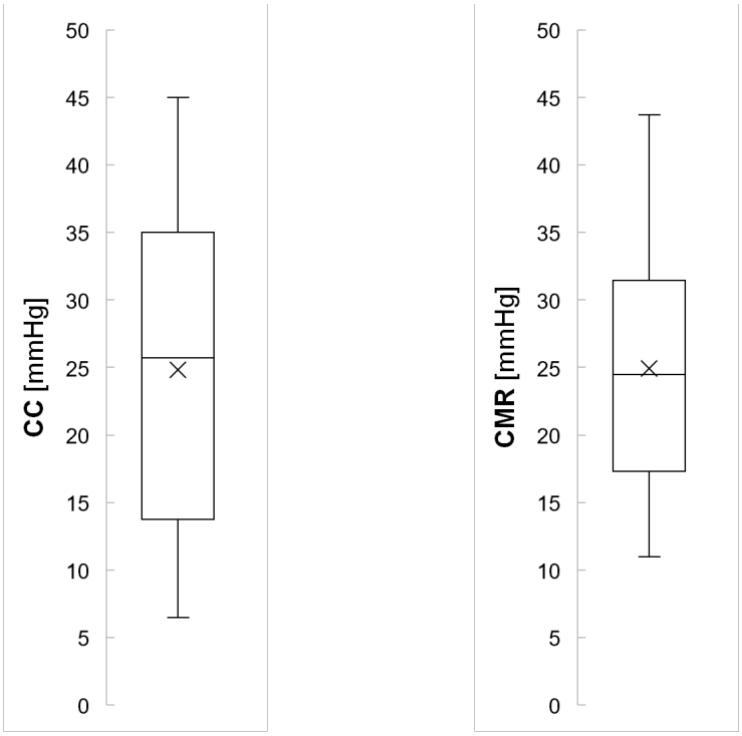

Figure 2. Box plots of peak-to-peak systolic gradients measured by cardiac catheterization (CC) and mean peak instantaneous pressure gradients measured by four-dimensional flow cardiovascular magnetic resonance (CMR) with median (solid line), mean (cross), interquartile range (box) and whiskers.

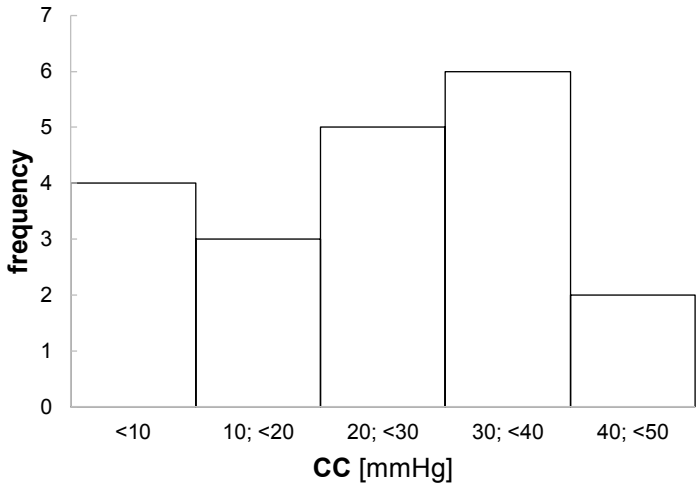

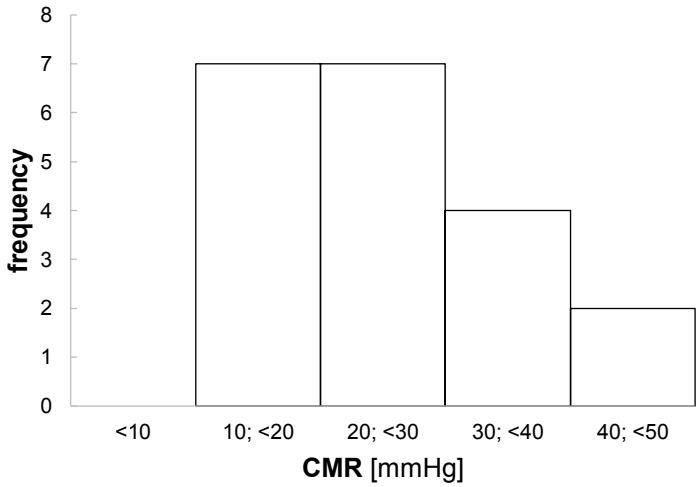

Figure 3. Histograms of peak-to-peak systolic gradients measured by cardiac catheterization (CC) and mean peak instantaneous pressure gradients measured by four-dimensional flow cardiovascular magnetic resonance (CMR).

9.3 Differences Between Cardiac Catheterization and Four-Dimensional Flow Cardiovascular Magnetic Resonance Measurements

Figure 4 and 5 both illustrate the distribution of differences between relative pressure gradient values measured by cardiac catheterization and 4D flow CMR.

Regarding the box plot, two values are outside the lower and upper inner fence. The lower and upper inner fence were calculated as follows:

$$\text{bottom of the box} - \text{interquartile range} \times 1.5$$

$$\text{top of the box} + \text{interquartile range} \times 1.5$$

Hence, two mild outliers can be identified. The interquartile range is small and spreads out symmetrically around the median and value zero.

The histogram of differences between peak-to-peak systolic gradient and mean peak instantaneous pressure gradient values is gaussian. Also, the kurtosis is relatively high what indicates that the variance of differences results from more extreme but less frequent values.

Two normality tests were performed to further assess the likelihood that the differences between relative pressure gradient values come from a normal distribution. Therefore, a Shapiro-Wilk and Kolmogorow-Smirnow test were conducted with the statistical analysis software SPSS Statistics version 22, provided by IBM Corporation in Armonk, United States. Results for the two normality tests indicate that differences between relative pressure gradient values are normally distributed. The null hypothesis that differences between relative pressure gradient values are normally distributed could not be rejected (p-value > 0.05).

In the synopsis of graphical analysis and normality test results, the distribution of differences between measurements is found to be normal. No outliers are excluded, and a parametric approach is used to estimate measurement agreement.

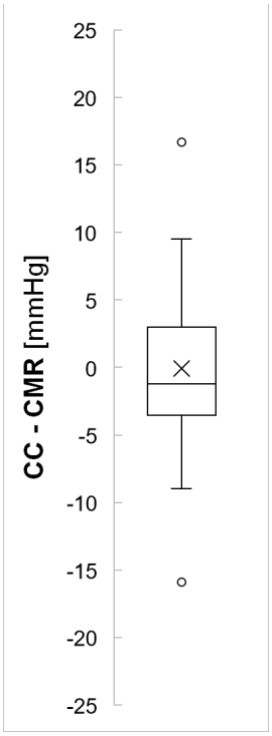

Figure 4. Box plot of differences between relative pressure gradients measured by cardiac catheterization (CC) and four-dimensional flow cardiovascular magnetic resonance (CMR) with median (solid line), mean (cross), interquartile range (box), whiskers and outliers (dots).

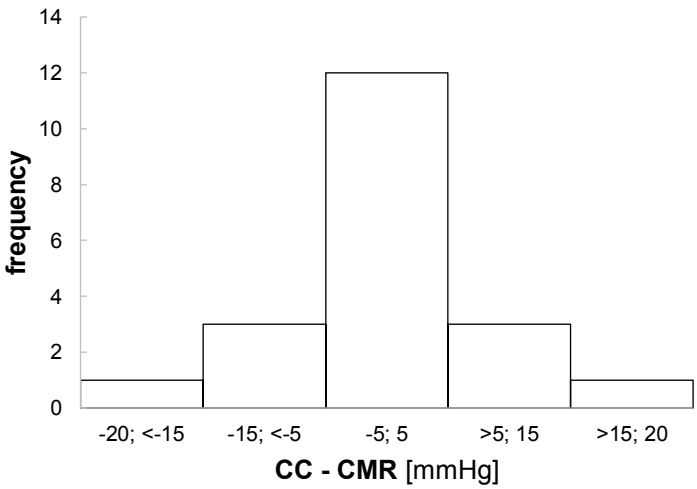

Figure 5. Histogram of differences between relative pressure gradients measured by cardiac catheterization (CC) and four-dimensional flow cardiovascular magnetic resonance (CMR).

9.4 Agreement Between Cardiac Cathertization and Four-Dimensional Flow Cardiovascular Magnetic Resonance Measurements

Agreement between measurements by cardiac catheterization and 4D flow CMR is graphically illustrated in figure 6 and 7 and is mainly estimated based on publications from Bland, JM and Altman, DG. Furthermore, a test of equivalence was performed. Additionally, a non-parametric approach is used. Agreement was estimated without the interpretation of correlation coefficients, linear regression methods as well as hypothesis testing because it is not necessary in this case of statistical analysis and can lead to incorrect conclusions (Bland & Altman, 1986, 1990, 1995a, 1995b, 1999, 2003).

The range of clinical irrelevant deviation for relative pressure gradient estimation was set to ±5 mmHg. The range of clinical irrelevant deviation stands for a difference between measurements by the two methods that will not lead to diagnostic errors in most of patients being investigated.

Moura and colleagues analyzed the “reproducibility of echocardiography measurements in valvular aortic valve stenosis”. Again, echocardiography is “the key tool for the diagnosis and evaluation of valve disease” (Baumgartner et al., 2009). To do so, TTEs were obtained in 150 patients with asymptomatic moderate aortic stenosis by two blinded observers at two different times. Moura et al. found the coefficient of reproducibility for interobserver variability for peak instantaneous pressure gradient measurements to be 5.58 mmHg. The coefficient of reproducibility provides an interval in relation to the mean of differences. Within this interval 95% of differences between two observers will lie when measuring peak instantaneous pressure gradients in the same patient with TTE (Moura, Ramos, Pinto, Barros, & Rocha-Goncalves, 2011). On grounds of the study results, the range of clinical irrelevant deviation for relative pressure gradient estimation was set to ±5 mmHg for the following statistical analysis.

Figure 6 shows matching peak-to-peak systolic gradient and mean peak instantaneous pressure gradient values plotted against each other. The dashed line represents the line of equality or identity line. The line of

equality will be the line all points lie on, if the two methods measure the same identical relative pressure gradient value for every observation.

Approximately, points lie symmetrically on both sides of the equality line regardless of the relative pressure gradient magnitude. Despite a reduced point density and missing data for peak-to-peak systolic gradient values > 45 mmHg, the influence of a systematic error is small and/or contributing effects to a systematic error neutralize. The distribution of points mostly reflects random error with a rather large variance.

Figure 7 additionally describes the quantitative aspect of agreement between the two methods in relation to the average of measured values. Although, the reference method for relative pressure gradient estimation was used for this comparison study, the true value of each relative pressure gradient remains unknown because the reference method does not guarantee that the method works without measurement error. Therefore, differences are plotted against the average of values measured by cardiac catheterization and 4D flow CMR instead of a single cardiac catheterization measurement value. In this sense, the mean of measurements is the best guess for an unknown true relative pressure gradient value. Furthermore, plotting differences against the average of values of the reference and new method is less prone to a false interpretation of agreement in relation to the magnitude of measurements. According to Bland and Altman “a plot of the difference[s] against the average of the standard and new method is unlikely […] to show a relation between difference[s] and magnitude when there is none” (Bland & Altman, 1995a).

Again, the distribution of points in relation to the relative pressure gradient magnitude is approximately symmetric on both sides of the horizontal zero-line. The variance of differences is homogenous across the range of measurement. Hence, the level of agreement is independent of the relative pressure gradient magnitude < 45 mmHg.

The dashed line represents the mean difference between measurements by the two methods also referred to as systematic error or bias. The bias is -0.1 mmHg. The bias is calculated as follows (Bland & Altman, 1999):

$$\text{peak} - \text{to} - \text{peak systolic pressure gradients}_{\text{averaged}} - \text{mean peak instantaneous pressure gradients}_{\text{averaged}}$$

A -0.1 mmHg bias further indicates that the influence of a systematic error is small and/or contributing effects to a systematic error neutralize under the present measurement conditions.

The variance of the bias can be estimated by the SD of the differences. The SD of the differences is 7.2 mmHg. The solid lines represent the 95% limits of agreement. The limits define a range in which 95% of all differences between measurements by the two methods will lie, if the differences are normally distributed. The limits of agreement are -14.2 to 14 mmHg. The limits were calculate as follows (Bland & Altman, 1999):

$$\text{bias} \pm 1.96 \times \text{SD}_{\text{of differences}}$$

The 95% confidence interval (CI) for the lower limit is -21.7 to -6.3 mmHg and 6.5 to 21.9 mmHg for the upper limit. The CIs were calculated as follows (Bland & Altman, 2003):

$$\text{limits of agreement} \pm 1.96 \times \sqrt{3 \times \frac{\text{SD}^2_{\text{of differences}}}{\text{number of subjects}}}$$

CIs for the 95% limits of agreement are extensive mostly due to the small number of included subjects.

To estimate equivalence, a CI for the differences between relative pressure gradient values, measured by the two methods, was calculated. In this approach to estimate measurement agreement, equivalence is approved if the two-sided 95% CI lies entirely inside the predefined range of clinical irrelevant deviation for relative pressure gradient estimation, which is also known as range of equivalence. The two-sided 95% CI was calculated by a paired t-test (SPSS Statistics, version 22, IBM

Corporation, Armonk, United States) and is -3.5 to 3.3 mmHg. The CI lies entirely inside the predefined range of equivalence. Hence the two methods can be described as equivalent in regard of the mean difference between relative pressure gradient values. Also, the value zero is within the 95% CI. Hence, the mean difference between relative pressure gradient values is non-significant.

Additionally, a non-parametric approach is used to estimate agreement, suggested by the British Hypertension Society in their protocol for validation of blood pressure measuring devices in adults (O'Brien et al., 2002). This approach is simply an array of percentage values of rounded and absolute differences within certain limits. No outliers are excluded, although the approach is considered non-parametric. Of all rounded and absolute differences between peak-to-peak systolic gradient and mean peak instantaneous pressure gradient values 70% are ≤ 5 mmHg, 90% are ≤ 10 mmHg and 10% are > 15 mmHg, as displayed in table 12.

Table 12. Summary of non-invasive pressure gradient estimation based on rounded and absolute differences between measurements by cardiac catheterization and four-dimensional flow cardiovascular magnetic resonance.

Limit [mmHg]	≤ 5	≤ 10	≤ 15
Proportion of rounded and absolute differences [pct.]	70	90	90

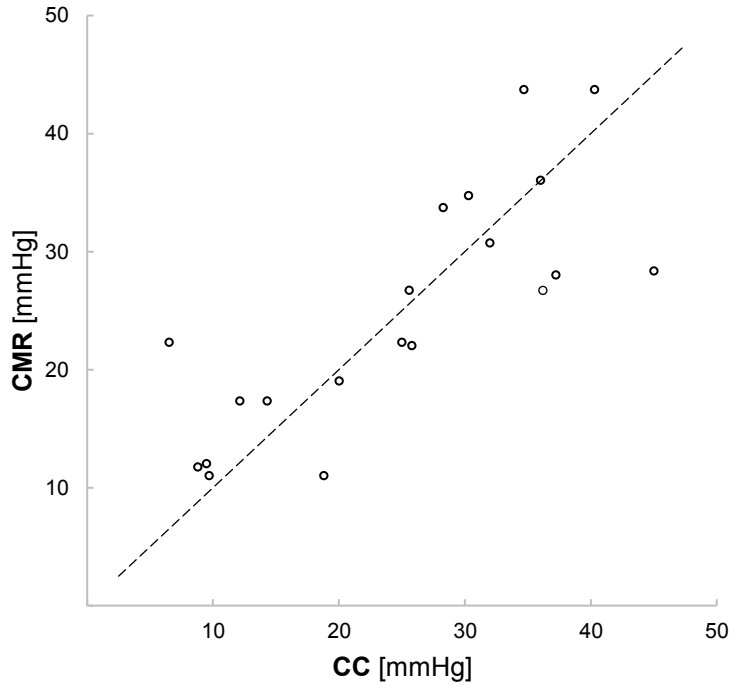

Figure 6. Relativ pressure gradients measured by cardiac catheterization (CC) and four-dimensional flow cardiovascular magnetic resonance (CMR) with line of equality (dashed line).

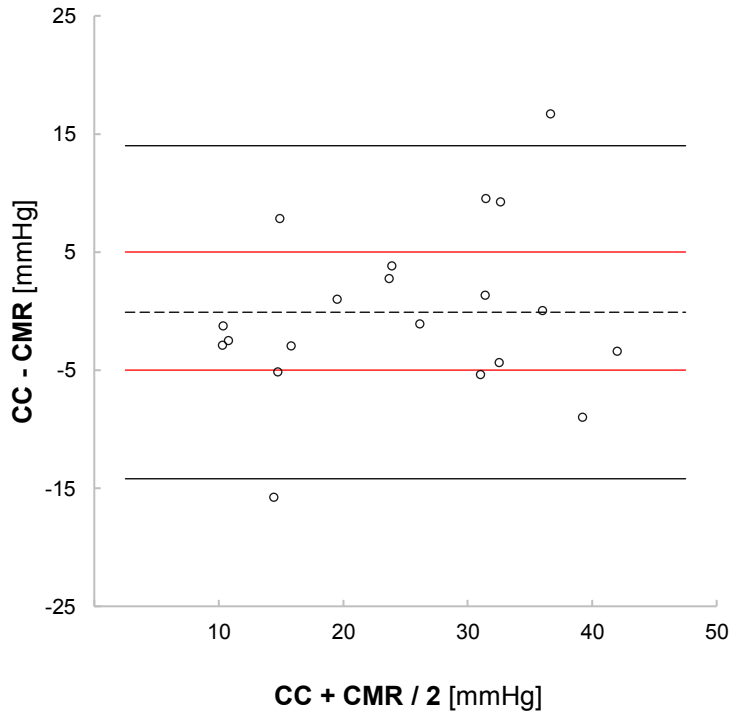

Figure 7. Relative pressure gradient differences versus average of values measured by cardiac catheterization (CC) and four-dimensional flow cardiovascular magnetic resonance (CMR) with 95% limits of agreement (black solid lines), range of clinical irrelevant deviation (red solid lines) and bias (dashed line).

10 Discussion

Measurement agreement is determined by subjects, observers and used methods and all three factors can interfere with its quality. When we want to measure a clinical quantity, with a new method because the new method has a competitive advantage over the standard method, then we need to know if the two methods can be used interchangeably, so that the patient can benefit without a loss in measurement quality. Before methods can be used interchangeably, a certain level of agreement must be proven in a sufficiently large and representative study population. This level of agreement is predefined by limits of clinical irrelevant deviation, which on the other hand stand for a difference between measurements by the two methods that will not lead to diagnostic errors in most of the observations. Studies to estimate measurement agreement between two methods must fulfill certain criteria, so results are affected as little as possible by subjects and/or observers. Therefore, methods should measure the same quantity, in the same subject, repeatedly, independently and simultaneously or under equal measurement conditions.

The main terms to describe measurement quality are accuracy and precision. Accuracy means the ability of a method to give a correct estimate of a quantity. Accuracy is estimated by the difference between a measurement value and a true value of a quantity and is a different expression for systematic error or bias. Precision stands for the degree of distribution of several measurement values collected by a method, which tries to give correct estimates of a true value of a quantity. Precision is estimated by a measure of variability and is a different expression for random error or repeatability. Similarly, measurement agreement between methods is described and estimated.

4D flow CMR data to estimate relative pressure gradients can be exploited in different ways. Therefore, measurement results eventually are dependent on type of algorithms and how they are implemented by software vendors.

The basis of a correct relative pressure gradient estimation by such implemented algorithms is a 4D flow CMR data acquisition with high quality. The key characteristics regarding quality of 4D flow CMR data acquisition are a sufficient spatiotemporal resolution and a suitable

velocity-encoding gradient (Nasiraei-Moghaddam et al., 2004). In PC imaging velocities are averaged across the dimension of a voxel and the duration of gradient application. A low spatial resolution leads to an underestimation of velocities and consequentially relative pressure gradients due to partial volume effects, especially in voxels located at the vessel wall as well as at the boundary of the vena contracta. Spatial resolution in clinical application of 4D flow CMR is ultimately restricted by scan time. In this study, the median voxel size inside the mean acquisition volume of 6.24 l is 2.5 × 2.34 × 2.34 mm^3 (2.1 to 2.5 × 1.8 to 2.5 × 1.8 to 2.5) and was generated in 9.8 minutes on average. A spatial resolution > 1.5 mm^3 already causes a significant underestimation of relative pressure gradient values calculated by the NSE and PPE (Casas, Lantz, Dyverfeldt, & Ebbers, 2016).

Lotz et al. report a significant underestimation of velocities for a temporal resolution < 11 frames per cardiac cycle (Lotz et al., 2002). In this study, the temporal resolution was sufficiently covered with an average of 19 frames per patient.

Regarding the velocity-encoding gradient magnitude across stenotic lesions, a VENC cannot be set in an arbitrary way and must be adjusted to the expected maximum velocity of the vena contracta to prevent phase aliasing. A high VENC is suitable for maximum velocities of the vena contracta but makes for a mismatch of minimum velocities around the obstructive lesion. This mismatch of velocity-encoding and the resulting poor velocity-to-noise ratio leads to an underestimation of velocities. Noise can be reduced by a multi-VENC overlapping scheme derived from several 4D flow scans with different velocity-encoding gradients (Ha et al., 2016) or other techniques. Unfortunately, underestimation of velocities is inevitable for a single-VENC acquisition of higher grade stenoses. In the end, correct 4D flow data acquisition is a matter of time and results in a trade-off between short scan time and high image quality.

In their 2009 publication, Ebbers and Farnebäck point out that the PPE implementation is not straightforward since results depend on the shape of the vessel and the computational domain as a copy of the anatomy (Ebbers & Farneback, 2009). Yet, the finite element solver of the PPE used in this study seems to be robust towards different vessel geometries

like the aortic arch and bifurcation of the MPA. In fact, Casas et al. suggest that the PPE could be more useful for relative pressure gradient estimation in complex vessel geometries than the Bernoulli methods (Casas et al., 2016).

The relative pressure field calculated by the NSE, is the derivate of the acquired velocity field by 4D flow CMR and the segmentation of cardiovascular compartments defines how much of the velocity field is assigned to the computational domain. Hence, the process of segmentation is significant for the final results, while the reliability of the semiautomatic segmentation process depends crucially on the generated ratio between signal intensity magnitude as well as PC and the amount of noise in 4D flow CMR data sets. Segmentation of ROIs with a laminar and homogenous flow only requires some user interaction and final 3D models are easy to reproduce, with similar as well as anatomically correct vessel boundaries. This is not the case for areas with a turbulent and inhomogeneous flow. A turbulent flow leads to different velocities within voxels in the area distal to higher grade stenoses. The range of velocities or velocity fluctuation inside a voxel produces a range of phases, which in turn alters the voltage induction during TE and causes a deprivation of signal intensity magnitudes (Oshinski, Ku, & Pettigrew, 1995).

Regarding image contrast in patients with higher grade stenoses, it makes for a difference if the ROI is segmented based on magnitude images, PC images or a combination of the two. Usually patient specific time-averaged PC MRAs are used for segmentation. A time-averaged PC MRA combines information about absolute velocities and signal magnitude. The weighting between PC and magnitude images is constant over the range of measurement of relative pressure gradients and does not account for the changing contrast ratio between the two image types in patients with higher grade stenoses. Consequently, segmentation requires more user interaction. Therefore, results are less precise or reproducible as well as anatomically correct in patients with higher grade stenoses, due to signal loss as well as lower PC in poststenotic areas. According to Bock and colleagues, administration of contrast agent significantly helps to improve the signal-to-noise ratio of 4D flow CMR data in healthy volunteers (Bock et al., 2010). In this study, no contrast

agents were used to decrease noise and increase signal intensity in patients prior to 4D flow acquisitions.

Furthermore, the pulsatile movement of vessel boundaries is neglected because time-averaged PC MRAs are not time-resolved and the exact position of vessel boundaries over the cardiac cycle is unknown. This is a problem because relative pressure gradient computation with the PPE is sensitive about errors close to the vessel boundaries (Meier et al., 2013). One straightforward solution to overcome this, which was not used in this study, is to morphologically erode the final 3D model after segmentation about 1 to 2 voxels.

The signal loss in 4D flow CMR data due to turbulent flow represents viscous dissipation of energy into heat as well as acoustic noise and can be correlated with transvalvular pressure losses. To do so, the amount of energy loss or turbulent flow intensity is estimated by the SD of velocity distribution within voxels (Dyverfeldt et al., 2013; Dyverfeldt, Sigfridsson, Kvitting, & Ebbers, 2006). The NSE do not account for energy dissipation on grounds of turbulent flow because only mean velocities are used as input. Therefore, according to Casas and colleagues, NSE and PPE solver are not capable to compute irreversible or true transvalvular pressure losses. The authors justify their statement based on in vitro CFD and PC-MRI simulations. Results show that relative pressure gradients between two points up- and downstream in relation to a stenosis computed by NSE and PPE solver do not agree with simulated reference values of true transvalvular pressure gradients. On the other hand, maximum pressure gradients at the level of the stenosis computed by NSE and PPE solver have a good agreement compared to true transvalvular pressure gradients (bias: 1.4 mmHg; 95% limits of agreement: -2.8 to 5.5 mmHg) (Casas et al., 2016).

Additionally, PPE solver do not account for viscous energy loss due to non-turbulent flow patterns. Non-turbulent energy loss can be estimated separately based on 4D flow CMR data by a reformulation of the viscous portion of the NSE (Barker et al., 2014).

Clinical acceptance of diagnostic methods is also determined by ease of use. Image reconstruction of the extensive amount of 4D flow CMR data per patient takes several minutes. Software tools to correct and analyze

4D flow CMR data are not integrated into PACS. The data transfer from PACS workstations to a personal computer is merely ensured by portable storage mediums and takes up to five minutes. The process of phase offset and phase aliasing correction requires less than five minutes approximately. Relative pressure gradient computation by the NSE and PPE with a finite element solver is fast. In fact, what is primarily compromising convenience of 4D flow CMR data processing is the 3D segmentation of ROIs. Scan time is mainly determined by user settings. Moreover, scan time and image quality are particularly depending on the patient's heart as well as breathing rhythm and frequency. Another inconvenience or challenge is the anticipation of maximum velocities in the ROI and to make a correct adjustment for a suitable VENC.

The range of clinical irrelevant deviation, to estimate agreement of relative pressure gradient measurements, was set to ±5 mmHg based on the study results from Moura et al. Moura and colleagues found the reproducibility coefficient, to quantify inter-observer variability of peak instantaneous pressure gradient measurements by TTE in 150 patients with moderate valvular aortic valve stenosis, to be 5.58 mmHg (Moura et al., 2011). The particular range of clinical irrelevant deviation might be acceptable for patients with RVOT obstruction. In patients with RVOT obstruction intervention is recommended when the peak instantaneous pressure gradient measured by TTE is > 64 mmHg, given that the RV contractility is still preserved and no valve replacement is needed (Baumgartner et al., 2010). Otherwise, in patients with aortic coarctation intervention is recommended when the peak-to-peak systolic gradient measured by cardiac catheterization is > 20 mmHg (Baumgartner et al., 2010). In this patient group, the set up range of clinical irrelevant deviation would already account for 50% of the interventional pressure gradient threshold value, compared to 15.6% for patients with RVOT obstruction.

Riesenkampff and colleagues investigated relative pressure gradients across aortic coarctations in 13 patients with NSE and PPE solver. They report a bias between invasive peak-to-peak systolic gradients measured by cardiac catheterization and non-invasive peak-to-peak systolic gradients measured by 4D flow CMR of 1.5 mmHg and 95% limits of agreement from -3.1 to 6.1 mmHg (Riesenkampff et al., 2014). Compared

to this study, measurement conditions were equal in terms of sedation as well as the implemented NSE and PPE solver. Measurement conditions were different regarding the retrospective study design, measurement site, administration of contrast agents during CMR scans, a narrower as well as lower range of measurement, ROI segmentation and the presence of shunts as well as regurgitation. Additionally, there is no statement about repeatability of at least one of the two measurement methods. The minor underestimation of relative pressure gradients by 4D flow CMR is consistent with the method's intrinsic general underestimation described in earlier publications (Bock et al., 2011; Ebbers & Farneback, 2009; Meier et al., 2013). Underestimation might be even bigger under more equal measurement conditions regarding the sedation bias. The narrow limits of agreement might result from the prospective study design with a better accordance between cardiac catheterization measurement points and measurement points inside each ROI as well as more equal hemodynamics of patients during procedures.

10.1 Limitations

Some limitations of this study must be considered. First, data was analyzed retrospectively. Consequentially, there was no information available about the basic hemodynamics of patients throughout CMR examinations, which could have been compared with blood pressure readings standardly recorded during cardiac catheterization procedures. This is important to note because apart from lesion morphology, which is considered as constant over a period of one day, relative pressure gradient magnitudes depend on cardiac output and vascular resistance.

Moreover, the exact positions of measurement points during cardiac catheterization procedures remain unknown because no more detailed definition was agreed on other than RV, LPA and RPA. This is crucial since the effect of catheter positioning on the variability of relative pressure gradient magnitude is substantial (Assey, Zile, Usher, Karavan, & Carabello, 1993) due to proximal pressure loss (Laskey & Kussmaul, 2001) and distal pressure recovery close to obstructive lesions (Laskey & Kussmaul, 1994).

Furthermore, measurement conditions were not equal in terms of sedation and administration of pharmaceuticals since only 4D flow data sets generated without sedation were used for comparison. One would have expected a systematic overestimation of relative pressure gradients by CMR measurements because the RV cardiac output and pulmonary vascular resistance of patients during scans were not compromised by sedatives (Hammarén & Hynynen, 1995) and pharmaceuticals.

Additionally, measurement point printouts from pressure curves recorded in the catheter laboratory were not superimposed to calculate peak instantaneous pressure gradients. Instead, manually sized non-synchronous peak-to-peak systolic gradients were used for comparison. Currie and colleagues report an overestimation of peak-to-peak systolic gradients by peak instantaneous pressure gradients across RVOT obstructive lesions both measured by cardiac catheterization in their correlative study about Doppler and dual catheter pressure gradient measurements. Again, one would have expected a systematic overestimation of relative pressure gradients by CMR measurements because of the reported mean difference of 11% between peak

instantaneous pressure gradients and peak-to-peak systolic gradients measured by cardiac catheterization (Currie et al., 1986).

Another important aspect that was not sufficiently addressed, is the comparison of repeatability or precision of the two methods. According to Bland and Altman, agreement is determined by the variation of repeated measurements or replicates by two methods on the same subject. For example, if the repeatability of the standard method is poor, a new method with better repeatability will not have a good agreement in comparison (Bland & Altman, 1999).

Therefore, repeatability must be estimated together with measurement agreement in method comparison studies. In other words, information about the repeatability of each method is required as a reference to estimate precision between methods. Replicates stand for more than one measurement by the same method, on the same subject, under the same conditions and independent from each other or blinded on previous measurement values. Replicates can be hard to obtain in clinical practice. In terms of cardiac catheterization measurements, repeated catheterizations to assess the precision of the method cannot be justified. Otherwise, repeated probing of measurement points during a single cardiac catheterization procedure is imaginable. Repeated 4D flow CMR scans certainly have a time penalty that cannot be easily overcome with a one-hour time slot per patient. However, a single data set can be evaluated repeatedly by several segmentations of a ROI or software tools with different algorithms for relative pressure gradient estimation. Since measurement points were probed just once in the catheter laboratory, only one peak-to-peak systolic gradient between the RV and LPA as well as one peak-to-peak systolic gradient between the RV and RPA could be calculated per patient. On the contrary, three peak instantaneous pressure gradients between the RV and LPA as well as three peak instantaneous pressure gradients between the RV and RPA could be generated with the 4D flow analysis software per data set. Therefore, comparison of repeatability of each method could only be evaluated to a limited degree.

A further shortcoming relates to the segmentation process of ROIs in time-averaged PC MRAs of 4D flow CMR data sets. As already

mentioned, relative pressure gradient estimation by 4D flow CMR is determined by the number and location of voxels semiautomatically assigned to the computational domain. Since the segmentation process is observer dependent, especially in patients with higher grade stenoses, evaluation of 4D flow data sets must have been blinded on peak-to-peak systolic gradient values since the magnitude of peak instantaneous pressure gradient values can be manipulated to a certain extend by how much of the velocity field is included into the computational domain by segmentation.

Finally, the last drawback of this study is the small sample size. The degree of reliability by which a study result is transferable to the general population is ultimately depending on the sample size of a study. Moreover, the study population must cover a wider range of measurement with peak-to-peak systolic gradient values > 45 mmHg to prove that the method can meet the full spectrum of clinical requirements. Both aspects need to be considered but most certainly suffers the study from little data.

10.2 Summary

In this study, agreement between peak-to-peak systolic gradients measured by cardiac catheterization and peak instantaneous pressure gradients measured by four-dimensional (4D) flow cardiovascular magnetic resonance (CMR) using the Navier-Stokes and Pressure Poisson equations was estimated retrospectively.

Included patients (n=10) were examined at the Klinik für Kinderkardiologie und Angeborene Herzfehler, Deutsches Herzzentrum München because of obstructive and/or insufficient pulmonary valves or homografts. Patients present a broad spectrum of congenital heart disease, with either a primary or secondary impairment of the right ventricle outflow tract. For each patient, relative pressure gradients between the right ventricle and left pulmonary artery as well as the right ventricle and right pulmonary artery were measured by the two methods, respectively. All patients were scanned one day ahead or on the same day prior to cardiac catheterization procedures. 4D flow scans were performed without sedation and without administration of contrast agents. The median spatiotemporal resolution of 4D flow CMR acquisitions is 2.5 × 2.34 × 2.34 mm^3 (2.1 to 2.5 × 1.8 to 2.5 × 1.8 to 2.5) and 38.4 ms (36.9 to 40). The range of measurement for peak-to-peak systolic gradients is 6 to 45 mmHg with a median of 26 mmHg. The median regurgitation in main pulmonary arteries or homografts is 22% with a 0 to 62% range. The median shunt ratio between the pulmonary and systemic circulation is 1:1 with a 0.7 to 1.2:1 range.

Differences between measurements by cardiac catheterization and 4D flow CMR are normally distributed. The comparison of measurements indicates a moderate to good agreement between the two methods. Results show that 95% of all differences between the two methods will lie within -14.2 (95% CI: -21.7 to -6.3) to 14 mmHg (95% CI: 6.5 to 21.9). The 95% limits of agreement are not congruent with the predefined ±5 mmHg limits of clinical irrelevant deviation. Nonetheless, 70% of 4D flow CMR measurements have a clinical irrelevant deviation of ±5 mmHg or less and 90% have a deviation of less than ±10 mmHg compared to cardiac catheterization measurements. Against this, 10% have an extensive deviation of more than ±15 mmHg.

4D flow CMR gives accurate estimates of relative pressure gradients compared to cardiac catheterization with a mean difference between measurements or bias of -0.1 mmHg (95% CI: -3.5 to 3.3 mmHg). A marginal bias indicates that the influence of a systematic error is small and/or contributing effects to a systematic error neutralize under the present measurement conditions.

The 95% confidence interval for the mean difference of measurements lies entirely inside the predefined ±5 mmHg range of clinical irrelevant deviation. Hence, the two methods can be described as equivalent. Additionally, the 95% confidence interval includes the value zero. Therefore, the differences between the two methods are non-significant. Furthermore, the graphical presentation of results indicates that the accuracy and precision of the 4D flow CMR method is supposably independent of relative pressure gradient magnitudes < 45 mmHg.

The intraobserver coefficient of repeatability for the software analysis of 4D flow CMR data sets is 4.9 mmHg. Repeatability of cardiac catheterization measurements was not evaluated. If the limits of agreement are congruent with the range ±repeatability coefficient of at least one of the two methods, then a lack of precision will be explained by a lack of repeatability of the corresponding method. In this study, the lack of precision between the two methods is not explained by a lack of repeatability of 4D flow CMR software analysis, since the limits of agreement are not congruent with the range of ±4.9 mmHg. Apart from this, reasons for the extensive limits of agreement cannot be further restricted.

10.3 Conclusion

To our knowledge, estimation of relative pressure gradients by 4D flow CMR, using the Navier-Stokes and Pressure Poisson equations, compared to cardiac catheterization measurements, has been described for the first time in patients with a primary or secondary impairment of the right ventricle outflow tract due to congenital heart disease. Relative pressure gradient estimation, using the Navier-Stokes and Pressure Poisson equations on grounds of a velocity field generated with 4D flow CMR, has proven its feasibility. The non-invasive and comprehensive diagnostic abilities of 4D flow CMR are promising for patients with congenital heart disease in terms of research and clinical application.

Based on results from this study, cardiac catheterization and 4D flow CMR cannot be used interchangeably to estimate relative pressure gradients in patients with mild to moderate obstructive lesions of the right ventricle outflow tract caused by congenital heart disease. Nevertheless, accuracy and precision of 4D flow CMR regarding relative pressure gradient estimation, using the Navier-Stokes and Pressure Poisson equations, compared to cardiac catheterization need to be further investigated. Future studies must take replicates by both methods under more equal measurement conditions, focus on the full range of measurement and include more patients.

11 Abstract

Introduction: Pressure gradients serve to grade the severity of obstructive valvular conditions. To measure pressure gradients correctly and at best in a non-harmful way is crucial for the initial treatment and long-term follow-up of affected patients. Cardiac catheterization (CC) is the reference method for measurements of pressure gradients. CC was used to estimate the accuracy and precision of relative pressure gradient measurements by four-dimensional (4D) flow cardiovascular magnetic resonance (CMR), between the right ventricle and both pulmonary arteries, in patients with a primary or secondary impairment of the right ventricular outflow tract due to congenital heart disease.

Methods: 10 patients were included. Patients were scanned without sedation and without administration of contrast agents. The median time difference between CC and 4D flow CMR procedures is 1 day (0 to 1). The median spatiotemporal resolution of 4D flow CMR acquisitions is 2.5 × 2.34 × 2.34 mm^3 (2.1 to 2.5 × 1.8 to 2.5 × 1.8 to 2.5) and 38.4 ms (36.9 to 40). Accuracy and precision were estimated retrospectively between peak-to-peak systolic gradients measured by CC and peak instantaneous pressure gradients computed by the Navier-Stokes as well as Pressure Poisson equations. The median peak-to-peak systolic gradient is 26 mmHg (6.5 to 45). The median regurgitation in main pulmonary arteries or homografts is 22% (0 to 62). The median shunt ratio is 1:1 (0.7 to 1.2:1).

Results: Of all rounded and absolute differences between peak-to-peak and peak instantaneous pressure gradients 70% are ≤ 5 mmHg, 90% are ≤ 10 mmHg and 10% are > 15 mmHg. The 95% limits of agreement are -14.2 (95% CI: -21.7 to -6.3) to 14 mmHg (95% CI: 6.5 to 21.9). The bias is -0.1 mmHg (95% CI: -3.5 to 3.3 mmHg). The intraobserver coefficient of repeatability for the software analysis of 4D flow CMR data sets is 4.9 mmHg.

Conclusion: The two methods show a moderate to good agreement. 70% of rounded and absolute differences have a clinical irrelevant deviation of ≤ 5 mmHg. 4D flow CMR gives accurate estimates compared to CC and differences between methods are non-significant. However, the two methods cannot be used interchangeably due to a lack of precision. Pressure gradient estimation by 4D flow CMR has proven its

feasibility. The non-invasive and comprehensive diagnostic abilities of 4D flow CMR are promising for patients with congenital heart disease in terms of research and clinical application.

Einleitung: Druckgradienten dienen dazu den Schweregrad von obstruktiven Herzklappenerkrankungen zu bestimmen. Druckgradienten genau zu messen und im besten Fall ohne dabei Schaden zu verursachen, ist von entscheidender Bedeutung bei der initialen Behandlung und langfristigen Nachsorge von betroffenen Patienten. Für die Bestimmung von Druckgradienten gilt der Herzkatheter (HK) als die Referenzmethode. Ergebnisse aus dem HK wurden genutzt um die Genauigkeit und Präzision in Bezug auf Druckgradienten zu beurteilen, die mit einer vierdimensionalen (4D) Fluss Magnetresonanztomographie (MRT) gemessen wurden, zwischen dem rechten Ventrikel und beiden Pulmonalarterien, in Patienten mit einer primären oder sekundären Beeinträchtigung des rechtsventrikulären Ausflusstraktes aufgrund von angeborenen Herzfehlern.

Methoden: 10 Patienten wurden eingeschlossen. Die Patienten wurden gescannt ohne Sedierung und ohne die Gabe von Kontrastmitteln. Im Mittel langen die HK und 4D Fluss MRT Untersuchungen 1 Tag (0 bis 1) auseinander. Die mediane räumliche und zeitliche Auflösung der 4D Fluss MRT Untersuchungen beträgt 2.5 × 2.34 × 2.34 mm^3 (2.1 bis 2.5 × 1.8 bis 2.5 × 1.8 bis 2.5) und 38.4 ms (36.9 bis 40). Die Messübereinstimmung wurde retrospektive bestimmt zwischen peak-to-peak Druckgradienten gemessen im HK und peak instantaneous Druckgradienten berechnet durch die Navier-Stokes und Pressure Poisson Gleichungen. Der mediane peak-to-peak Druckgradient liegt bei 26 mmHg (6,5 bis 45). Die mediane Regurgitation im Stamm der Pulmonalarterie oder dem homologen Transplantat beträgt 22% (0 bis 62). Das mediane Shunt-Verhältnis ist 1:1 (0,7 bis 1,2:1).

Ergebnisse: Von allen gerundeten und absoluten Differenzen zwischen den peak-to-peak und peak instantaneous Druckgradienten sind 70% ≤ 5 mmHg, 90% ≤ 10 mmHg und 10% > 15 mmHg. Die 95% Grenzen der Übereinstimmung liegen bei -14.2 (95% KI: -21.7 bis -6.3) und 14 mmHg (95% KI: 6.5 bis 21.9). Die mittlere Differenz liegt bei -0.1 mmHg (95% KI: -3.5 bis 3.3 mmHg). Der Wiederholungs-Koeffizient für die Software-Analyse der Datensätze der 4D Fluss MRT Untersuchungen durch einen Untersucher liegt bei 4.9 mmHg.

Fazit: Die zwei Methoden zeigen eine moderate bis gute Übereinstimmung. 70% der gerundeten und absoluten Differenzen haben eine klinisch irrelevante Abweichung von ≤ 5 mmHg. Die 4D Fluss MRT liefert genaue Messwerte verglichen mit dem HK und die Messunterschiede zwischen den Methoden sind nicht signifikant. Dennoch kann die 4D Fluss MRT den HK nicht ersetzen, aufgrund mangelnder Präzision in der Übereinstimmung. Die 4D Fluss MRT hat ihre Durchführbarkeit in Bezug auf die Messung von Druckgradienten unter Beweis gestellt und die nicht invasiven als auch umfassenden diagnostischen Möglichkeiten der 4D Fluss MRT sind vielversprechend für Patienten mit angeborenen Herzfehlern in Bezug auf Forschung und klinische Anwendung.

Figures

FIGURE 1. FICTITIOUS PRESSURE CURVE OF A MEASUREMENT POINT PRINTOUT WITH MEAN PEAK SYSTOLIC PRESSURE VALUE (DASHED LINE) AND STANDARD DEVIATION OF PEAK SYSTOLIC PRESSURE VALUES (SOLID LINES). 44

FIGURE 2. BOX PLOTS OF PEAK-TO-PEAK SYSTOLIC GRADIENTS MEASURED BY CARDIAC CATHETERIZATION (CC) AND MEAN PEAK INSTANTANEOUS PRESSURE GRADIENTS MEASURED BY FOUR-DIMENSIONAL FLOW CARDIOVASCULAR MAGNETIC RESONANCE (CMR) WITH MEDIAN (SOLID LINE), MEAN (CROSS), INTERQUARTILE RANGE (BOX) AND WHISKERS. 54

FIGURE 3. HISTOGRAMS OF PEAK-TO-PEAK SYSTOLIC GRADIENTS MEASURED BY CARDIAC CATHETERIZATION (CC) AND MEAN PEAK INSTANTANEOUS PRESSURE GRADIENTS MEASURED BY FOUR-DIMENSIONAL FLOW CARDIOVASCULAR MAGNETIC RESONANCE (CMR). 55

FIGURE 4. BOX PLOT OF DIFFERENCES BETWEEN RELATIVE PRESSURE GRADIENTS MEASURED BY CARDIAC CATHETERIZATION (CC) AND FOUR-DIMENSIONAL FLOW CARDIOVASCULAR MAGNETIC RESONANCE (CMR) WITH MEDIAN (SOLID LINE), MEAN (CROSS), INTERQUARTILE RANGE (BOX), WHISKERS AND OUTLIERS (DOTS). 57

FIGURE 5. HISTOGRAM OF DIFFERENCES BETWEEN RELATIVE PRESSURE GRADIENTS MEASURED BY CARDIAC CATHETERIZATION (CC) AND FOUR-DIMENSIONAL FLOW CARDIOVASCULAR MAGNETIC RESONANCE (CMR). 57

FIGURE 6. RELATIV PRESSURE GRADIENTS MEASURED BY CARDIAC CATHETERIZATION (CC) AND FOUR-DIMENSIONAL FLOW CARDIOVASCULAR MAGNETIC RESONANCE (CMR) WITH LINE OF EQUALITY (DASHED LINE). 62

FIGURE 7. RELATIVE PRESSURE GRADIENT DIFFERENCES VERSUS AVERAGE OF VALUES MEASURED BY CARDIAC CATHETERIZATION (CC) AND FOUR-DIMENSIONAL FLOW CARDIOVASCULAR MAGNETIC RESONANCE (CMR) WITH 95% LIMITS OF AGREEMENT (BLACK SOLID LINES), RANGE OF CLINICAL IRRELEVANT DEVIATION (RED SOLID LINES) AND BIAS (DASHED LINE). 62

Tables

TABLE 1. INCLUSION CRITERIA. 37

TABLE 2. EXCLUSION CRITERIA. 37

TABLE 3. SCAN PARAMETER. 40

TABLE 4. HARDWARE. 45

TABLE 5. SOFTWARE. 45

TABLE 6. PHARMACEUTICALS USED DURING CARDIAC CATHETERIZATION PROCEDURES. 46

TABLE 7. PHARMACEUTICALS USED DURING CARDIOVASCULAR MAGNETIC RESONANCE PROCEDURES. 46

TABLE 8. REASONS WHY PATIENTS WERE NOT INCLUDED. 47

TABLE 9. PATIENT CHARACTERISTICS. 49

TABLE 10. MEDICAL RECORDS. 50

TABLE 11. RESULTS. 53

TABLE 12. SUMMARY OF NON-INVASIVE PRESSURE GRADIENT ESTIMATION BASED ON ROUNDED AND ABSOLUTE DIFFERENCES BETWEEN MEASUREMENTS BY CARDIAC CATHETERIZATION AND FOUR-DIMENSIONAL FLOW CARDIOVASCULAR MAGNETIC RESONANCE. 61

References

Akcakaya, M., Gulaka, P., Basha, T. A., Ngo, L. H., Manning, W. J., & Nezafat, R. (2014). Free-breathing phase contrast MRI with near 100% respiratory navigator efficiency using k-space-dependent respiratory gating. *Magn Reson Med, 71*(6), 2172-2179. doi:10.1002/mrm.24874

Akins, C. W., Travis, B., & Yoganathan, A. P. (2008). Energy loss for evaluating heart valve performance. *J Thorac Cardiovasc Surg, 136*(4), 820-833. doi:10.1016/j.jtcvs.2007.12.059

Assey, M. E., Zile, M. R., Usher, B. W., Karavan, M. P., & Carabello, B. A. (1993). Effect of catheter positioning on the variability of measured gradient in aortic stenosis. *Catheterization and Cardiovascular Diagnosis, 30*(4), 287–292. doi:10.1002/ccd.1810300405

Babu-Narayan, S. V., Giannakoulas, G., Valente, A. M., Li, W., & Gatzoulis, M. A. (2015). Imaging of congenital heart disease in adults. *Eur Heart J*. doi:10.1093/eurheartj/ehv519

Barker, A. J., van Ooij, P., Bandi, K., Garcia, J., Albaghdadi, M., McCarthy, P., Bonow, R. O., Carr, J., Collins, J., Malaisrie, S. C., Markl, M. (2014). Viscous energy loss in the presence of abnormal aortic flow. *Magn Reson Med, 72*(3), 620-628. doi:10.1002/mrm.24962

Baumgartner, H., Bonhoeffer, P., De Groot, N. M., de Haan, F., Deanfield, J. E., Galie, N., Gatzoulis M. A., Gohlke-Baerwolf, C., Kaemmerer, H., Kilner, P., Meijboom, F., Mulder, B. J., Oechslin, E., Oliver, J. M., Serraf, A., Szatmari, A., Thaulow, E., Vouhe, P. R., Walma, E. (2010). ESC Guidelines for the management of grown-up congenital heart disease (new version 2010). *Eur Heart J, 31*(23), 2915-2957. doi:10.1093/eurheartj/ehq249

Baumgartner, H., Hung, J., Bermejo, J., Chambers, J. B., Evangelista, A., Griffin, B. P., Iung, B., Otto, C. M., Pellikka, P. A., Quiñones, M. (2009). Echocardiographic assessment of valve stenosis: EAE/ASE recommendations for clinical practice. *Eur J Echocardiogr, 10*(1), 1-25. doi:10.1093/ejechocard/jen303

Beausejour Ladouceur, V., Lawler, P. R., Gurvitz, M., Pilote, L., Eisenberg, M. J., Ionescu-Ittu, R., Guo, L., Marelli, A. J. (2016). Exposure to Low-Dose Ionizing Radiation From Cardiac Procedures in Patients With Congenital Heart Disease: 15-Year Data From a Population-Based Longitudinal Cohort. *Circulation, 133*(1), 12-20. doi:10.1161/CIRCULATIONAHA.115.019137

Bergersen, L., Marshall, A., Gauvreau, K., Beekman, R., Hirsch, R., Foerster, S., Balzer, D., Vincent, J., Hellenbrand, W., Holzer, R., Cheatham, J., Moore, J., Lock, J., Jenkins, K. (2010). Adverse event rates in congenital cardiac catheterization - a multi-center experience. *Catheter Cardiovasc Interv, 75*(3), 389-400. doi:10.1002/ccd.22266

Bernstein, M. A., Zhou, X. J., Polzin, J. A., King, K. F., Ganin, A., Pelc, N. J., & Glover, G. H. (1998). Concomitant gradient terms in phase contrast MR: Analysis and correction. *Magn Reson Med, 39*(2), 300–308. doi:10.1002/mrm.1910390218

Bland, J. M., & Altman, D. G. (1986). Statistical methods for assessing agreement between two methods of clinical measurement. *Lancet, 327*(8476), 307-310. doi:10.1016/S0140-6736(86)90837-8

Bland, J. M., & Altman, D. G. (1990). A note on the use of the intraclass correlation coefficient in the evaluation of agreement between two methods of measurement. *20, 5*, 337-340. doi:10.1016/0010-4825(90)90013-F

Bland, J. M., & Altman, D. G. (1995a). Comparing methods of measurement: why plotting difference against standard method is misleading. *Lancet, 346*(8982), 1085-1087. doi:10.1016/S0140-6736(95)91748-9

Bland, J. M., & Altman, D. G. (1995b). Comparing Two Methods of Clinical Measurement: A Personal History. *International Journal of Epidemiology, 24*(Supplement_1), S7-S14. doi:10.1093/ije/24.Supplement_1.S7

Bland, J. M., & Altman, D. G. (1999). Measuring Agreement in Method Comparison Studies. *Statistical Methods in Medical Research, 8*(2), 135-160. doi:10.1177/096228029900800204

Bland, J. M., & Altman, D. G. (2003). Applying the right statistics: analyses of measurement studies. *Ultrasound Obstet Gynecol, 22*(1), 85-93. doi:10.1002/uog.122

Bock, J., Frydrychowicz, A., Lorenz, R., Hirtler, D., Barker, A. J., Johnson, K. M., Arnold, R., Burkhardt, H., Hennig, J., Markl, M. (2011). In vivo noninvasive 4D pressure difference mapping in the human aorta: phantom comparison and application in healthy volunteers and patients. *Magn Reson Med, 66*(4), 1079-1088. doi:10.1002/mrm.22907

Bock, J., Frydrychowicz, A., Stalder, A. F., Bley, T. A., Burkhardt, H., Hennig, J., & Markl, M. (2010). 4D phase contrast MRI at 3 T: effect of standard and blood-pool contrast agents on SNR, PC-MRA, and blood flow visualization. *Magn Reson Med, 63*(2), 330-338. doi:10.1002/mrm.22199

Brix, G., Kolem, H., Nitz, W. R., Bock, M., Huppertz, A., Zech, C. J., & Dietrich, O. (2008). Basics of Magnetic Resonance Imaging and Magnetic Resonance Spectroscopy. In M. F. Reiser, W. Semmler, & H. Hricak (Eds.), *Magnetic Resonance Tomography* (pp. 3-167). Berlin, Heidelberg: Springer.

Brown, R. W., Cheng, Y. N., Haacke, E. M., Thompson, M. R., & Venkatesan, R. (2014). *Magnetic Resonance Imaging: Physical Principles and Sequence Design* (2nd ed.): John Wiley & Sons.

Bryant, D. J., Payne, J. A., Firmin, D. N., & Longmore, D. B. (1984). Measurement of flow with NMR imaging using a gradient pulse and phase difference technique. *J Comput Assist Tomogr, 8*(4), 588-593.

Bushong, S. C., & Clarke, G. (2014). *Magnetic Resonance Imaging* (4th ed.): Mosby.

Calabrese, E. J. (2013). Low doses of radiation can enhance insect lifespans. *Biogerontology, 14*(4), 365-381. doi:10.1007/s10522-013-9436-5

Cardiovascular Catheterization and Intervention: A Textbook of Coronary, Peripheral, and Structural Heart Disease. (2010). (D. Mukherjee, E. Bates, M. Roffi, & D. Moliterno Eds. 1 ed.): Informa PLC.

Carr, H. Y., & Purcell, E. M. (1954). Effects of Diffusion on Free Precession in Nuclear Magnetic Resonance Experiments. *Phys. Rev., 94*(3). doi:10.1103/PhysRev.94.630

Carvalho, J. S., Moscoso, G., Tekay, A., Campbell, S., Thilaganathan, B., & Shinebourne, E. A. (2004). Clinical impact of first and early second trimester fetal echocardiography on high risk pregnancies. *Heart, 90*(8), 921-926. doi:10.1136/hrt.2003.015065

Casas, B., Lantz, J., Dyverfeldt, P., & Ebbers, T. (2016). 4D Flow MRI-based pressure loss estimation in stenotic flows: Evaluation using numerical simulations. *Magn Reson Med, 75*(4), 1808-1821. doi:10.1002/mrm.25772

Chai, P., & Mohiaddin, R. (2005). How We Perform Cardiovascular Magnetic Resonance Flow Assessment Using Phase Contrast Velocity Mapping. *J Cardiovasc Magn Reson, 7*(4). doi:10.1081/JCMR-65639

Chang, R. K., Rodriguez, S., Lee, M., & Klitzner, T. S. (2006). Risk factors for deaths occurring within 30 days and 1 year after hospital discharge for cardiac surgery among pediatric patients. *Am Heart J, 152*(2), 386-393. doi:10.1016/j.ahj.2005.12.016

Coogan, J. S., Humphrey, J. D., & Figueroa, C. A. (2013). Computational simulations of hemodynamic changes within thoracic, coronary, and cerebral arteries following early wall remodeling in response to distal aortic coarctation. *Biomech Model Mechanobiol, 12*(1), 79-93. doi:10.1007/s10237-012-0383-x

Currie, P. J., Seward, J. B., Fyfe, D. A., Bove, A. A., & Taji, J. (1986). Instantaneous pressure gradient: A simultaneous doppler and dual catheter correlative study. *JACC, 7*(4), 800-806. doi:10.1016/S0735-1097(86)80339-4

Davenport, M. S., Khalatbari, S., Cohan, R. H., & Ellis, J. H. (2013). Contrast Medium–induced Nephrotoxicity Risk Assessment in Adult Inpatients: A Comparison of Serum Creatinine Level– and Estimated Glomerular Filtration Rate–based Screening Methods. *Radiology, 269*(1), 92-100. doi:10.1148/radiol.13122462

Deshmane, A., Gulani, V., Griswold, M. A., & Seiberlich, N. (2012). Parallel MR imaging. *J Magn Reson Imaging, 36*(1), 55-72. doi:10.1002/jmri.23639

Diller, G. P., Dimopoulos, K., Okonko, D., Li, W., Babu-Narayan, S. V., Broberg, C. S., Johansson, B., Bouzas, B., Mullen, M. J., Poole-Wilson, P. A., Francis, D. P., Gatzoulis, M. A. (2005). Exercise intolerance in adult congenital heart disease: comparative severity, correlates, and prognostic implication. *Circulation, 112*(6), 828-835. doi:10.1161/CIRCULATIONAHA.104.529800

Donati, F., Figueroa, C. A., Smith, N. P., Lamata, P., & Nordsletten, D. A. (2015). Non-invasive pressure difference estimation from PC-MRI using the work-energy equation. *Med Image Anal, 26*(1), 159-172. doi:10.1016/j.media.2015.08.012

Dorfman, A. L., Levine, J. C., Colan, S. D., & Geva, T. (2005). Accuracy of echocardiography in low birth weight infants with congenital heart disease. *Pediatrics, 115*(1), 102-107. doi:10.1542/peds.2004-0147

Dyverfeldt, P., Bissell, M., Barker, A. J., Bolger, A. F., Carlhall, C. J., Ebbers, T., Francios, C. J., Frydrychowicz, A., Geiger, J., Giese, D., Hope, M. D., Kilner, P. J., Kozerke, S., Myerson, S., Neubauer, S., Wieben, O., Markl, M. (2015). 4D flow cardiovascular magnetic resonance consensus statement. *J Cardiovasc Magn Reson, 17*, 72. doi:10.1186/s12968-015-0174-5

Dyverfeldt, P., & Ebbers, T. (2017). Comparison of respiratory motion suppression techniques for 4D flow MRI. *Magn Reson Med*. doi:10.1002/mrm.26574

Dyverfeldt, P., Hope, M. D., Tseng, E. E., & Saloner, D. (2013). Magnetic resonance measurement of turbulent kinetic energy for the estimation of irreversible pressure loss in aortic stenosis. *JACC Cardiovasc Imaging, 6*(1), 64-71. doi:10.1016/j.jcmg.2012.07.017

Dyverfeldt, P., Sigfridsson, A., Kvitting, J. P., & Ebbers, T. (2006). Quantification of intravoxel velocity standard deviation and turbulence intensity by generalizing phase-contrast MRI. *Magnetic Resonance in Medicine, 56*(4), 850–858. doi:10.1002/mrm.21022

Dyvorne, H., Knight-Greenfield, A., Jajamovich, G., Besa, C., Cui, Y., Stalder, A., Markl, M., Taouli, B. (2015). Abdominal 4D Flow MR Imaging in a Breath Hold: Combination of Spiral Sampling and Dynamic Compressed Sensing for Highly Accelerated Acquisition. *Radiology, 275* (1), 245–254. doi:10.1148/radiol.14140973

Ebbers, T., & Farneback, G. (2009). Improving computation of cardiovascular relative pressure fields from velocity MRI. *J Magn Reson Imaging, 30*(1), 54-61. doi:10.1002/jmri.21775

Ebbers, T., Wigström, L., Bolger, A. F., Engvall, J., & Karlsson, M. (2001). Estimation of relative cardiovascular pressures using time-resolved three-dimensional phase contrast MRI. *Magn Reson Med, 45*(5), 872–879. doi:10.1002/mrm.1116

Eicken, A., Ewert, P., Hager, A., Peters, B., Fratz, S., Kuehne, T., Busch, R., Hess, J., Berger, F. (2011). Percutaneous pulmonary valve implantation: two-centre experience with more than 100 patients. *Eur Heart J, 32*(10), 1260-1265. doi:10.1093/eurheartj/ehq520

Ellis, J. H., Davenport, M. S., Dillman, J. R., Hartman, R. P., Herts, B. R., Jafri, S. Z., Kolbe, A. B., Laroia, A., Cohan, R. H., McDonald, R. J., Needleman, L., Newhouse, J. H., Pahade, J. K., Sirlin, C. B., Wang, C. L., Wasserman, N., Weinreb, J. C. (2015). ACR Manual on Contrast Media. *10.1*.

Engelfriet, P., Boersma, E., Oechslin, E., Tijssen, J., Gatzoulis, M. A., Thilen, U., Kaemmerer, H., Moons, P., Meijboom, F., Popelová, J., Laforest, V., Hirsch, R., Daliento, L., Thaulow, E., Mulder, B. (2005). The spectrum of adult congenital heart disease in Europe: morbidity and mortality in a 5 year follow-up period. The Euro Heart Survey on adult congenital heart disease. *Eur Heart J, 26*(21), 2325-2333. doi:10.1093/eurheartj/ehi396

Engelings, C. C., Helm, P. C., Abdul-Khaliq, H., Asfour, B., Bauer, U. M., Baumgartner, H., Kececioglu, D., Körten, M. A., Diller, G. P., Tutarel, O. (2016). Cause of death in adults with congenital heart disease - An analysis of the German National Register for Congenital Heart Defects. *Int J Cardiol, 211*, 31-36. doi:10.1016/j.ijcard.2016.02.133

Fatahi, M., Reddig, A., Vijayalaxmi, Friebe, B., Hartig, R., Prihoda, T. J., Ricke, J., Roggenbuck, D., Reinhold, D., Speck, O. (2016). DNA double-strand breaks and micronuclei in human blood lymphocytes after repeated whole body exposures to 7T Magnetic Resonance Imaging. *Neuroimage, 133*, 288-293. doi:10.1016/j.neuroimage.2016.03.023

Feltes, T. F., Bacha, E., Beekman, R. H., 3rd, Cheatham, J. P., Feinstein, J. A., Gomes, A. S., Hijazi, Z. M., Ing, F. F., de Moor, M., Morrow, W. R., Mullins, C. E., Taubert, K. A., Zahn, E. M. (2011). Indications for

cardiac catheterization and intervention in pediatric cardiac disease: a scientific statement from the American Heart Association. *Circulation, 123*(22), 2607-2652. doi:10.1161/CIR.0b013e31821b1f10

Firmin, D., & Keegan, J. (2001). Navigator Echoes in Cardiac Magnetic Resonance. *Journal of Cardiovascular Magnetic Resonance, 3*(3), 183-193. doi:10.1081/jcmr-100107467

Fratz, S., Chung, T., Greil, G. F., Samyn, M. M. A. M. T., E. R. Valsangiacomo Buechel, E. R., Shi-Joon Yoo, S.-J., & Powell, A. J. (2013). Guidelines and protocols for cardiovascular magnetic resonance in children and adults with congenital heart disease: SCMR expert consensus group on congenital heart disease. *Journal of Cardiovascular Magnetic Resonance, 15*(51). doi:10.1186/1532-429X-15-51

Gabbour, M., Rigsby, C., Markl, M., Schnell, S., Jarvis, K. B., de Freitas, R. A., Popescu, A. R., Robinson, J. D. (2013). Comparison of 4D flow and 2D PC MRI blood flow quantification in children and young adults with congenital heart disease. *J Cardiovasc Magn Reson, 15*. doi:10.1186/1532-429X-15-S1-E90

Glatz, A. C., Purrington, K. S., Klinger, A., King, A. R., Hellinger, J., Zhu, X., Gruber, S. B., Gruber, P. J. (2014). Cumulative exposure to medical radiation for children requiring surgery for congenital heart disease. *J Pediatr, 164*(4), 789-794 e710. doi:10.1016/j.jpeds.2013.10.074

Gorlin, R., & Gorlin, S. G. (1951). Hydraulic formula for calculation of the area of the stenotic mitral valve, other cardiac valves, and central circulatory shunts. I. *American Heart Journal, 41*(1), 1-29. doi:10.1016/0002-8703(51)90002-6

Goubergrits, L., Riesenkampff, E., Yevtushenko, P., Schaller, J., Kertzscher, U., Hennemuth, A., Berger, F., Schubert, S., Kuehne, T. (2015). MRI-based computational fluid dynamics for diagnosis and treatment prediction: clinical validation study in patients with coarctation of aorta. *J Magn Reson Imaging, 41*(4), 909-916. doi:10.1002/jmri.24639

Grainger, D. (2014). Safety Guidelines for Magnetic Resonance Imaging Equipment in Clinical Use. *Published by the Medicines and Healthcare Products Regulatory Agency*, 1-85.

Gratz, A., Hess, J., & Hager, A. (2009). Self-estimated physical functioning poorly predicts actual exercise capacity in adolescents and adults with congenital heart disease. *Eur Heart J, 30*(4), 497-504. doi:10.1093/eurheartj/ehn531

Griswold, M. A., Jakob, P. M., Heidemann, R. M., Nittka, M., Jellus, V., Wang, J., Kiefer, B., Haase, A. (2002). Generalized autocalibrating partially parallel acquisitions (GRAPPA). *Magn Reson Med, 47*(6), 1202-1210. doi:10.1002/mrm.10171

Ha, H., Kim, G. B., Kweon, J., Kim, Y. H., Kim, N., Yang, D. H., & Lee, S. J. (2016). Multi-VENC acquisition of four-dimensional phase-contrast MRI to improve precision of velocity field measurement. *Magn Reson Med, 75*(5), 1909-1919. doi:10.1002/mrm.25715

Hahn, E. L. (1960). Detection of sea-water motion by nuclear precession. *Journal of Geophysical Research, 65*(2), 776-777. doi:10.1029/JZ065i002p00776

Hamilton, J., Franson, D., & Seiberlich, N. (2017). Recent advances in parallel imaging for MRI. *Prog Nucl Magn Reson Spectrosc, 101*, 71-95. doi:10.1016/j.pnmrs.2017.04.002

Hammarén, E., & Hynynen, M. (1995). Haemodynamic effects of propofol infusion for sedation after coronary artery surgery. *BJA: British Journal of Anaesthesia, 75*(1), 47-50. doi:10.1093/bja/75.1.47

Han, B. K., Rigsby, C. K., Hlavacek, A., Leipsic, J., Nicol, E. D., Siegel, M. J., Bardo, D., Abbara, S., Ghoshhajra, B., Lesser, J. R., Raman, S., Crean, A. M. (2015). Computed Tomography Imaging in Patients with Congenital Heart Disease Part I: Rationale and Utility. An Expert Consensus Document of the Society of Cardiovascular Computed Tomography (SCCT): Endorsed by the Society of Pediatric Radiology (SPR) and the North American Society of Cardiac Imaging (NASCI). *Journal of Cardiovascular Computed Tomography, 9*(6), 475–492. doi:10.1016/j.jcct.2015.07.004

Hanneman, K., Kino, A., Cheng, J. Y., Alley, M. T., & Vasanawala, S. S. (2016). Assessment of the precision and reproducibility of ventricular volume, function, and mass measurements with ferumoxytol-enhanced 4D flow MRI. *J Magn Reson Imaging, 44*(2), 383-392. doi:10.1002/jmri.25180

Hoffman, J. I., & Kaplan, S. (2002). The Incidence of Congenital Heart Disease. *J Am Coll Cardiol, 39*(12), 1890-1900. doi:10.1016/S0735-1097(02)01886-7

Horwood, L., Attili, A., Luba, F., Ibrahim, E. H., Parmar, H., Stojanovska, J., Gadoth-Goodman, S., Fette, C., Oral, H., Bogun, F. (2016). Magnetic resonance imaging in patients with cardiac implanted electronic devices: focus on contraindications to magnetic resonance imaging protocols. *Europace*. doi:10.1093/europace/euw122

Huang, F., Akao, J., Vijayakumar, S., Duensing, G. R., & Limkeman, M. (2005). k-t GRAPPA: a k-space implementation for dynamic MRI with high reduction factor. *Magn Reson Med, 54*(5), 1172-1184. doi:10.1002/mrm.20641

ICRP. (2012). Statement on Tissue Reactions / Early and Late Effects of Radiation in Normal Tissues and Organs – Threshold Doses for Tissue Reactions in a Radiation Protection Context. *Ann. ICRP, 41*(1-2), 1-322. doi:10.1016/j.icrp.2012.02.001

ICRP. (2015). Stem Cell Biology with Respect to Carcinogenesis Aspects of Radiological Protection. *Ann. ICRP, 44*(3-4). doi:10.1177/0146645315595585

Jarvis, K., Vonder, M., Barker, A. J., Schnell, S., Rose, M., Carr, J., Robinson, J. D., Markl, M., Rigsby, C. K. (2016). Hemodynamic evaluation in patients with transposition of the great arteries after the arterial switch operation: 4D flow and 2D phase contrast cardiovascular magnetic resonance compared with Doppler echocardiography. *J Cardiovasc Magn Reson, 18*(1), 59. doi:10.1186/s12968-016-0276-8

Jayaram, N., Beekman, R. H., 3rd, Benson, L., Holzer, R., Jenkins, K., Kennedy, K. F., Martin, G. R., Moore, J. W., Ringel, R., Rome, J., Spertus, J. A., Vincent, R., Bergersen, L. (2015). Adjusting for Risk Associated With Pediatric and Congenital Cardiac Catheterization: A Report From the NCDR IMPACT Registry. *Circulation, 132*(20), 1863-1870. doi:10.1161/CIRCULATIONAHA.114.014694

Jenkinson, M. (2003). Fast, automated, N-dimensional phase-unwrapping algorithm. *Magn Reson Med, 49*(1), 193-197. doi:10.1002/mrm.10354

Johnson, J. N., Hornik, C. P., Li, J. S., Benjamin, D. K., Jr., Yoshizumi, T. T., Reiman, R. E., Frush, D. P., Hill, K. D. (2014). Cumulative radiation exposure and cancer risk estimation in children with heart disease. *Circulation, 130*(2), 161-167. doi:10.1161/CIRCULATIONAHA.113.005425

Johnson, K. M., Lum, D. P., Turski, P. A., Block, W. F., Mistretta, C. A., & Wieben, O. (2008). Improved 3D phase contrast MRI with off-resonance corrected dual echo VIPR. *Magn Reson Med, 60*(6), 1329-1336. doi:10.1002/mrm.21763

Jung, B., Ullmann, P., Honal, M., Bauer, S., Hennig, J., & Markl, M. (2008). Parallel MRI with extended and averaged GRAPPA kernels (PEAK-GRAPPA): optimized spatiotemporal dynamic imaging. *J Magn Reson Imaging, 28*(5), 1226-1232. doi:10.1002/jmri.21561

Kaemmerer, H., Bauer, U., Pensl, U., Oechslin, E., Gravenhorst, V., Franke, A., Hager, A., Balling, G., Hauser, M., Eicken, A., Hess, J. (2008). Management of emergencies in adults with congenital cardiac disease. *Am J Cardiol, 101*(4), 521-525. doi:10.1016/j.amjcard.2007.09.110

Kanal, E., Barkovich, A. J., Bell, C., Borgstede, J. P., Bradley, W. G., Froelich, J. W., Gimbel, J. R., Gosbee, J. W., Kuhni-Kaminski, E., Larson, P. A., Lester, J. W. Jr, Nyenhuis, J., Schaefer, D. J., Sebek, E. A., Weinreb, J., Wilkoff, B. L., Woods, T. O., Lucey, L., Hernandez, D. (2013). ACR Guidance Document on MR Safe Practices: 2013. *Journal of magnetic resonance imaging, 37*(3), 501-530. doi:10.1002/jmri.24011

Khairy, P., Ionescu-Ittu, R., Mackie, A. S., Abrahamowicz, M., Pilote, L., & Marelli, A. J. (2010). Changing mortality in congenital heart disease. *J Am Coll Cardiol, 56*(14), 1149-1157. doi:10.1016/j.jacc.2010.03.085

Khairy, P., Van Hare, G. F., Balaji, S., Berul, C. I., Cecchin, F., Cohen, M. I., Daniels, C. J., Deal. B. J., Dearani, J. A., Groot, Nd., Dubin, A. M., Harris, L., Janousek, J., Kanter, R. J., Karpawich, P. P., Perry, J. C., Seslar, S. P., Shah, M. J., Silka, M. J., Triedman, J. K., Walsh, E. P., Warnes, C. A. (2014). PACES/HRS Expert Consensus Statement on the Recognition and Management of Arrhythmias in Adult Congenital Heart Disease: developed in partnership between the Pediatric and Congenital Electrophysiology Society (PACES) and the Heart Rhythm Society (HRS). Endorsed by the governing bodies of PACES, HRS, the American College of Cardiology (ACC), the American Heart Association (AHA), the European Heart Rhythm Association (EHRA), the Canadian Heart Rhythm Society (CHRS), and the International Society for Adult Congenital Heart Disease (ISACHD). *Heart Rhythm, 11*(10), e102-165. doi:10.1016/j.hrthm.2014.05.009

Kilner, P. J., Manzara, C. C., Mohiaddin, R. H., Pennell, D. J., Sutton, M. G., Firmin, D. N., Underwood, S. R., Longmore, D. B. (1993). Magnetic resonance jet velocity mapping in mitral and aortic valve stenosis. *Circulation, 87*(4), 1239-1248. doi:10.1161/01.cir.87.4.1239

Koyak, Z., Harris, L., de Groot, J. R., Silversides, C. K., Oechslin, E. N., Bouma, B. J., Budts, W., Zwinderman, A. H., Van Gelder, I.C., Mulder, B. J.

(2012). Sudden cardiac death in adult congenital heart disease. *Circulation, 126*(16), 1944-1954. doi:10.1161/CIRCULATIONAHA.112.104786

Krittian, S. B., Lamata, P., Michler, C., Nordsletten, D. A., Bock, J., Bradley, C. P., Pitcher, A., Kilner, P. J., Markl, M., Smith, N. P. (2012). A finite-element approach to the direct computation of relative cardiovascular pressure from time-resolved MR velocity data. *Med Image Anal, 16*(5), 1029-1037. doi:10.1016/j.media.2012.04.003

Kupfahl, C., Honold, M., Meinhardt, G., Vogelsberg, H., Wagner, A., Mahrholdt, H., & Sechtem, U. (2004). Evaluation of aortic stenosis by cardiovascular magnetic resonance imaging: comparison with established routine clinical techniques. *Heart, 90*(8), 893-901. doi:10.1136/hrt.2003.022376

Lankhaar, J. W., Hofman, M. B., Marcus, J. T., Zwanenburg, J. J., Faes, T. J., & Vonk-Noordegraaf, A. (2005). Correction of phase offset errors in main pulmonary artery flow quantification. *J Magn Reson Imaging, 22*(1), 73-79. doi:10.1002/jmri.20361

Laskey, W. K., & Kussmaul, W. G. (1994). Pressure recovery in aortic valve stenosis. *Circulation, 89*(1), 116-121. doi:10.1161/01.CIR.89.1.116

Laskey, W. K., & Kussmaul, W. G. (2001). Subvalvular Gradients in Patients With Valvular Aortic Stenosis Prevalence, Magnitude, and Physiological Importance. *Circulation, 104*(9), 1019-1022. doi:10.1161/hc3401.095041

Lauterbur, P. C. (1973). Image Formation by Induced Local Interactions: Examples Employing Nuclear Magnetic Resonance. *nature, 242*, 190-191. doi:10.1038/242190a0

Lindinger, A., Schwedler, G., & Hense, H. W. (2010). Prevalence of congenital heart defects in newborns in Germany: Results of the first registration year of the PAN Study (July 2006 to June 2007). *Klin Padiatr. 222*(5), 321-6. doi: 10.1055/s-0030-1254155.

Loecher, M., Schrauben, E., Johnson, K. M., & Wieben, O. (2016). Phase unwrapping in 4D MR flow with a 4D single-step laplacian algorithm. *J Magn Reson Imaging, 43*(4), 833-842. doi:10.1002/jmri.25045

Lorenz, R., Bock, J., Snyder, J., Korvink, J. G., Jung, B. A., & Markl, M. (2014). Influence of eddy current, Maxwell and gradient field corrections on 3D flow visualization of 3D CINE PC-MRI data. *Magn Reson Med, 72*(1), 33-40. doi:10.1002/mrm.24885

Lotz, J., Meier, C., Leppert, A., & Galanski, M. (2002). Cardiovascular Flow Measurement with Phase-Contrast MR Imaging: Basic Facts and Implementation. *Radiographics, 22*(3), 651–671. doi:10.1148/radiographics.22.3.g02ma11651

Lowe, M. D., Plummer, C. J., Manisty, C. H., & Linker, N. J. (2015). Safe use of MRI in people with cardiac implantable electronic devices. *Heart, 101*(24), 1950-1953. doi:10.1136/heartjnl-2015-308495

Lustig, M., Donoho, D., & Pauly, J. M. (2007). Sparse MRI: The application of compressed sensing for rapid MR imaging. *Magn Reson Med, 58*(6), 1182-1195. doi:10.1002/mrm.21391

Marelli, A. J., Ionescu-Ittu, R., Mackie, A. S., Guo, L., Dendukuri, N., & Kaouache, M. (2014). Lifetime prevalence of congenital heart

disease in the general population from 2000 to 2010. *Circulation, 130*(9), 749-756. doi:10.1161/CIRCULATIONAHA.113.008396
Markl, M., Bammer, R., Alley, M. T., Elkins, C. J., Draney, M. T., Barnett, A., Moseley, M. E., Glover, G. H., Pelc, N. J. (2003). Generalized reconstruction of phase contrast MRI: analysis and correction of the effect of gradient field distortions. *Magn Reson Med, 50*(4), 791-801. doi:10.1002/mrm.10582
Markl, M., Chan, F. P., Alley, M. T., Wedding, K. L., Draney, M. T., Elkins, C. J., Parker, D. W., Wicker, R., Taylor, C. A., Herfkens, R. J., Pelc, N. J. (2003). Time-resolved three-dimensional phase-contrast MRI. *J Magn Reson Imaging, 17*(4), 499-506. doi:10.1002/jmri.10272
Markl, M., Frydrychowicz, A., Kozerke, S., Hope, M., & Wieben, O. (2012). 4D flow MRI. *J Magn Reson Imaging, 36*(5), 1015-1036. doi:10.1002/jmri.23632
Markl, M., Harloff, A., Bley, T. A., Zaitsev, M., Jung, B., Weigang, E., Langer, M., Hennig, J., Frydrychowicz, A. (2007). Time-resolved 3D MR velocity mapping at 3T: improved navigator-gated assessment of vascular anatomy and blood flow. *J Magn Reson Imaging, 25*(4), 824-831. doi:10.1002/jmri.20871
Markl, M., Kilner, P. J., & Ebbers, T. (2011). Comprehensive 4D velocity mapping of the heart and great vessels by cardiovascular magnetic resonance. *J Cardiovasc Magn Reson, 13*(7). doi:10.1186/1532-429X-13-7
Markl, M., Schnell, S., Wu, C., Bollache, E., Jarvis, K., Barker, A. J., Robinson, J. D., Rigsby, C. K. (2016). Advanced flow MRI: emerging techniques and applications. *Clin Radiol*. doi:10.1016/j.crad.2016.01.011
Mathews, J. D., Forsythe, A. V., Brady, Z., Butler, M. W., Goergen, S. K., Byrnes, G. B., Giles, G. G., Wallace, A. B., Anderson, P. R., Guiver, T. A., McGale, P., Cain, T. M., Dowty, J. G., Bickerstaffe, A. C., Darby, S. C. (2013). Cancer risk in 680,000 people exposed to computed tomography scans in childhood or adolescence: data linkage study of 11 million Australians. *BMJ, 346*, f2360. doi:10.1136/bmj.f2360
Meier, S., Hennemuth, A., Drexl, J., Bock, J., Jung, B., & Preusser, T. (2013). A Fast and Noise-Robust Method for Computation of Intravascular Pressure Difference Maps from 4D PC-MRI Data. *Statistical Atlases and Computational Models of the Heart. Imaging and Modelling Challenges, 7746*, 215-224. doi:10.1007/978-3-642-36961-2_25
Mirzaee, H., Henn, T., Krause, M. J., Goubergrits, L., Schumann, C., Neugebauer, M., Kuehne, T., Preusser, T., Hennemuth, A. (2017). MRI-based computational hemodynamics in patients with aortic coarctation using the lattice Boltzmann methods: Clinical validation study. *J Magn Reson Imaging, 45*(1), 139-146. doi:10.1002/jmri.25366
Monson, R. R., Cleaver, J. E., Bingham, E., Buffler, P. A., Cardis, E., Cox, R., Davis, S., Dewey, W. C., Gilbert, E. S., Kellerer, A. M., Krewski, D., Lindahl, T. R., Rowan, K. E., Sankaranarayanan, K., Schafer, D. W., Stefanski, L. A., Ullrich, R. L. (2006). Health Risks from Exposure to Low Levels of Ionizing Radiation: BEIR VII Phase 2. *The National Academies Press*, 1-424. doi:10.17226/11340
Montalescot, G., Sechtem, U., Achenbach, S., Andreotti, F., Arden, C., Budaj, A., Bugiardini, R., Crea, F., Cuisset, T., Di Mario, C., Ferreira, J. R.,

Gersh, B. J., Gitt, A. K., Hulot, J. S., Marx, N., Opie, L. H., Pfisterer, M., Prescott, E., Ruschitzka, F., Sabaté, M., Senior, R., Taggart, D. P., van der Wall, E. E., Vrints, C. J. (2013). 2013 ESC guidelines on the management of stable coronary artery disease: the Task Force on the management of stable coronary artery disease of the European Society of Cardiology. *Eur Heart J, 34*(38), 2949-3003. doi:10.1093/eurheartj/eht296. Epub 2013 Aug 30

Moura, L. M., Ramos, S. F., Pinto, F. J., Barros, I. M., & Rocha-Goncalves, F. (2011). Analysis of variability and reproducibility of echocardiography measurements in valvular aortic valve stenosis. *Rev Port Cardiol, 30*(1), 25-33.

Nasiraei-Moghaddam, A., Behrens, G., Fatouraee, N., Agarwal, R., Choi, E. T., & Amini, A. A. (2004). Factors affecting the accuracy of pressure measurements in vascular stenoses from phase-contrast MRI. *Magn Reson Med, 52*(2), 300-309. doi:10.1002/mrm.20152

Nazarian, S., Hansford, R., Rahsepar, A. A., Weltin, V., McVeigh, D., Gucuk Ipek, E., Kwan, A., Berger, R. D., Calkins, H., Lardo, A. C., Kraut, M. A., Kamel, I. R., Zimmerman, S. L., Halperin, H. R. (2017). Safety of Magnetic Resonance Imaging in Patients with Cardiac Devices. *New England Journal of Medicine, 377*(26), 2555-2564. doi:10.1056/NEJMoa1604267

Nieminen, H. P., Jokinen, E. V., & Sairanen, H. I. (2007). Causes of late deaths after pediatric cardiac surgery: a population-based study. *J Am Coll Cardiol, 50*(13), 1263-1271. doi:10.1016/j.jacc.2007.05.040

Nishimura, R. A., & Carabello, B. A. (2012). Hemodynamics in the cardiac catheterization laboratory of the 21st century. *Circulation, 125*(17), 2138-2150. doi:10.1161/CIRCULATIONAHA.111.060319

Nishimura, R. A., Otto, C. M., Bonow, R. O., Carabello, B. A., Erwin, J. P., 3rd, Guyton, R. A., Guyton, R. A., O'Gara, P. T., Ruiz. C. E., Skubas, N. J., Sorajja, P., Sundt, T. M. 3rd, Thomas, J. D. (2014). 2014 AHA/ACC guideline for the management of patients with valvular heart disease: a report of the American College of Cardiology/American Heart Association Task Force on Practice Guidelines. *J Am Coll Cardiol, 63*(22), e57-185. doi:10.1016/j.jacc.2014.02.536

Nordmeyer, S., Riesenkampff, E., Crelier, G., Khasheei, A., Schnackenburg, B., Berger, F., & Kuehne, T. (2010). Flow-sensitive four-dimensional cine magnetic resonance imaging for offline blood flow quantification in multiple vessels: a validation study. *J Magn Reson Imaging, 32*(3), 677-683. doi:10.1002/jmri.22280

O'Brien, E., Pickering, T., Asmar, R., Myers, M., Parati, G., Staessen, J., Mengden, T., Imai, Y., Waeber, B., Palatini, P., Gerin, W. (2002). Working Group on Blood Pressure Monitoring of the European Society of Hypertension International Protocol for validation of blood pressure measuring devices in adults. *Blood Pressure Monitoring, 7*(1), 3-17.

Oshinski, J. N., Ku, D. N., & Pettigrew, R. I. (1995). Turbulent fluctuation velocity: the most significant determinant of signal loss in stenotic vessels. *Magnetic Resonance in Medicine, 33*(2), 193-199. doi:10.1002/mrm.1910330208

Pelc, N. J., Bernstein, M. A., Shimakawa, A., & Glover, G. H. (1991). Encoding strategies for three-direction phase-contrast MR imaging of flow. *J Magn Reson Imaging, 1*(4), 405–413. doi:10.1002/jmri.1880010404

Preston, D. L., Ron, E., Tokuoka, S., Funamoto, S., Nishi, N., Soda, M., Mabuchi, K., Kodama, K. (2007). Solid cancer incidence in atomic bomb survivors: 1958-1998. *Radiat Res, 168*(1), 1-64. doi:10.1667/RR0763.1

Pruessmann, K. P., Weiger, M., Scheidegger, M. B., & Boesiger, P. (1999). SENSE: sensitivity encoding for fast MRI. *Magn Reson Med, 42*(5), 952-962. doi:10.1002/(SICI)1522-2594(199911)42:5<952::AID-MRM16>3.0.CO;2-S

Riesenkampff, E., Fernandes, J. F., Meier, S., Goubergrits, L., Kropf, S., Schubert, S., Berger, F., Hennemuth, A., Kuehne, T. (2014). Pressure fields by flow-sensitive, 4D, velocity-encoded CMR in patients with aortic coarctation. *JACC Cardiovasc Imaging, 7*(9), 920-926. doi:10.1016/j.jcmg.2014.03.017

Ruskin, J., Bache, R. J., Rembert, J. C., & Greenfield, J. C. (1973). Pressure-Flow Studies in Man: Effect of Respiration on LeftVentricularStrokeVolume. *Circulation, 48*(1), 79-85. doi:10.1161/01.CIR.48.1.79

Russo, R. J. (2013). Determining the risks of clinically indicated nonthoracic magnetic resonance imaging at 1.5 T for patients with pacemakers and implantable cardioverter-defibrillators: rationale and design of the MagnaSafe Registry. *Am Heart J, 165*(3), 266-272. doi:10.1016/j.ahj.2012.12.004

Russo, R. J., Costa, H. S., Silva, P. D., Anderson, J. L., Arshad, A., Biederman, R. W., Boyle, N. G., Frabizzio, J. V., Birgersdotter-Green, U., Higgins, S. L., Lampert, R., Machado, C. E., Martin, E. T., Rivard, A. L., Rubenstein, J. C., Schaerf, R. H., Schwartz, J. D., Shah, D. J., Tomassoni, G. F., Tominaga, G. T., Tonkin, A. E., Uretsky, S., Wolff, S. D. (2017). Assessing the Risks Associated with MRI in Patients with a Pacemaker or Defibrillator. *N Engl J Med, 376*(8), 755-764. doi:10.1056/NEJMoa1603265

Santelli, C., Nezafat, R., Goddu, B., Manning, W. J., Smink, J., Kozerke, S., & Peters, D. C. (2011). Respiratory bellows revisited for motion compensation: preliminary experience for cardiovascular MR. *Magn Reson Med, 65*(4), 1097-1102. doi:10.1002/mrm.22687

Schaefer, D. J., Bourland, J. D., & Nyenhuis, J. A. (2000). Review of Patient Safety in Time‐Varying Gradient Fields. *J Magn Reson Imaging, 12*(1), 20-29.

Schenck, J. F. (2000). Safety of Strong, Static Magnetic Fields. *J Magn Reson Imaging, 12*(1), 2-19.

Schlichting , H., & Gersten, K. (2017). Onset of Turbulence (Stability Theory) *Boundary-Layer Theory* (pp. 415-496). Berlin, Heidelberg: Springer Berlin Heidelberg.

Shellock, F. G. (2000). Radiofrequency Energy‐Induced Heating During MR Procedures: A Review. *J Magn Reson Imaging, 12*(1), 30-36.

Sigfridsson, A., Petersson, S., Carlhall, C. J., & Ebbers, T. (2012). Four-dimensional flow MRI using spiral acquisition. *Magn Reson Med, 68*(4), 1065-1073. doi:10.1002/mrm.23297

Sokolov, M., & Neumann, R. (2016). Global Gene Expression Alterations as a Crucial Constituent of Human Cell Response to Low Doses of Ionizing Radiation Exposure. *Int J Mol Sci, 17*(1). doi:10.3390/ijms17010055

Stout, K. K., Broberg, C. S., Book, W. M., Cecchin, F., Chen, J. M., Dimopoulos, K., Everitt, M. D., Gatzoulis, M., Harris, L., Hsu, D. T., Kuvin, J. T., Law, Y., Martin, C. M., Murphy, A. M., Ross, H. J., Singh, G., Spray, T. L. (2016). Chronic Heart Failure in Congenital Heart Disease: A Scientific Statement From the American Heart Association. *Circulation, 133*(8), 770-801. doi:10.1161/CIR.0000000000000352

Tang, F. R., Loke, W. K., & Khoo, B. C. (2017). Low-dose or low-dose-rate ionizing radiation-induced bioeffects in animal models. *J Radiat Res*. doi:10.1093/jrr/rrw120

Todd, D. J., & Kay, J. (2016). Gadolinium-Induced Fibrosis. *Annu Rev Med, 67*, 273-291. doi:10.1146/annurev-med-063014-124936

Travers, J. G., Kamal, F. A., Robbins, J., Yutzey, K. E., & Blaxall, B. C. (2016). Cardiac Fibrosis: The Fibroblast Awakens. *Circ Res, 118*(6), 1021-1040. doi:10.1161/CIRCRESAHA.115.306565

Tsao, J., Boesiger, P., & Pruessmann, K. P. (2003). k-t BLAST and k-t SENSE: dynamic MRI with high frame rate exploiting spatiotemporal correlations. *Magn Reson Med, 50*(5), 1031-1042. doi:10.1002/mrm.10611

Tubiana, M. (2005). Dose-effect relationship and estimation of the carcinogenic effects of low doses of ionizing radiation: the joint report of the Academie des Sciences (Paris) and of the Academie Nationale de Medecine. *Int J Radiat Oncol Biol Phys, 63*(2), 317-319. doi:10.1016/j.ijrobp.2005.06.013

Tyszka, J. M., Laidlaw, D. H., Asa, J. A., & Silverman, J. M. (2000). Three-dimensional, time-resolved (4D) relative pressure mapping using magnetic resonance imaging. *J Magn Reson Imaging, 12*(2), 321–329. doi:10.1002/1522-2586(200008)12:2<321::AID-JMRI15>3.0.CO;2-2

UNSCEAR. (2012). Biological mechanisms of radiation actions at low doses. A white paper to guide the Scientific Committee's future programme of work.

Uribe, S., Beerbaum, P., Sorensen, T. S., Rasmusson, A., Razavi, R., & Schaeffter, T. (2009). Four-dimensional (4D) flow of the whole heart and great vessels using real-time respiratory self-gating. *Magn Reson Med, 62*(4), 984-992. doi:10.1002/mrm.22090

Vahanian, A., Alfieri, O., Andreotti, F., Antunes, M. J., Baron-Esquivias, G., Baumgartner, H., Borger, M. A., Carrel, T. P., De Bonis, M., Evangelista, A., Falk, V., Iung, B., Lancellotti, P., Pierard, L., Price, S., Schäfers, H. J., Schuler, G., Stepinska, J., Swedberg, K., Takkenberg, J., Von Oppell, U. O., Windecker, S., Zamorano, J. L., Zembala, M. (2012). Guidelines on the management of valvular heart disease (version 2012). *Eur Heart J, 33*(19), 2451-2496. doi:10.1093/eurheartj/ehs109

Valenti, V., Sciarretta, S., Levin, M., Shubayev, L., Edelstein, S., Zia, M. I., Rubattu, S., Volpe, M., Uretsky, S., Wolff, S. D. (2015). An easy and reproducible parameter for the assessment of the pressure gradient

in patients with aortic stenosis disease: A magnetic resonance study. *J Cardiol, 65*(5), 369-376. doi:10.1016/j.jjcc.2014.07.015

Valsangiacomo Buechel, E. R., Grosse-Wortmann, L., Fratz, S., Eichhorn, J., Sarikouch, S., Greil, G. F., Beerbaum, P., Bucciarelli-Ducci, C., Bonello, B., Sieverding, L., Schwitter, J., Helbing, W. A., Galderisi, M., Miller, O., Sicari, R., Rosa, J., Thaulow, E., Edvardsen, T., Brockmeier, K., Qureshi, S., Stein, J. (2015). Indications for cardiovascular magnetic resonance in children with congenital and acquired heart disease: an expert consensus paper of the Imaging Working Group of the AEPC and the Cardiovascular Magnetic Resonance Section of the EACVI. *Eur Heart J Cardiovasc Imaging, 16*(3), 281-297. doi:10.1093/ehjci/jeu129

van Ooij, P., Semaan, E., Schnell, S., Giri, S., Stankovic, Z., Carr, J., Barker, A. J., Markl, M. (2015). Improved respiratory navigator gating for thoracic 4D flow MRI. *Magn Reson Imaging, 33*(8), 992-999. doi:10.1016/j.mri.2015.04.008

Verheugt, C. L., Uiterwaal, C. S., van der Velde, E. T., Meijboom, F. J., Pieper, P. G., van Dijk, A. P., Vliegen, H. W., Grobbee, D. E., Mulder, B. J. (2010). Mortality in adult congenital heart disease. *Eur Heart J, 31*(10), 1220-1229. doi:10.1093/eurheartj/ehq032

Walker, P. G., Cranney, G. B., Scheidegger, M. B., Waseleski, G., Pohost, G. M., & Yoganathan, A. P. (1993). Semiautomated method for noise reduction and background phase error correction in MR phase velocity data. *J Magn Reson Imaging, 3*(3), 521–530. doi:10.1002/jmri.1880030315

Walsh, E. P., & Cecchin, F. (2007). Arrhythmias in adult patients with congenital heart disease. *Circulation, 115*(4), 534-545. doi:10.1161/CIRCULATIONAHA.105.592410

Wang, Y., Rossman, P. J., Grimm, R. C., Wilman, A. H., Riederer, S. J., & Ehman, R. L. (1996). 3D MR angiography of pulmonary arteries using realtime navigator gating and magnetization preparation. *Magn Reson Med, 36*(4), 579–587. doi:10.1002/mrm.1910360413

Warnes, C. A., Williams, R. G., Bashore, T. M., Child, J. S., Connolly, H. M., Dearani, J. A., Del Nido, P., Fasules, J. W., Graham, T. P. Jr, Hijazi, Z. M., Hunt, S. A., King, M. E., Landzberg, M. J., Miner, P. D., Radford, M. J., Walsh, E. P. (2008). ACC/AHA 2008 guidelines for the management of adults with congenital heart disease: a report of the American College of Cardiology/American Heart Association Task Force on Practice Guidelines. *J Am Coll Cardiol, 52*(23), e143-263. doi:10.1016/j.jacc.2008.10.001

WHO. (2016). International Statistical Classification of Diseases and Related Health Problems 10th Revision.

Wong, S., Spina, R., Toemoe, S., & Dhital, K. (2015). Is cardiac magnetic resonance imaging as accurate as echocardiography in the assessment of aortic valve stenosis? *Interact Cardiovasc Thorac Surg*. doi:10.1093/icvts/ivv362

Xiang, Q. S. (1995). Temporal phase unwrapping for cine velocity imaging. *J Magn Reson Imaging, 5*(5), 529-534. doi:10.1002/jmri.1880050509

Yang, G. Z., Kilner, P. J., Wood, N. B., Underwood, R. S., & Firmin, D. N. (1996). Computation of flow pressure fields from magnetic

resonance velocity map- ping. *Magn Reson Med, 36*(4), 520–526. doi:10.1002/mrm.1910360404

Mein besonderer Dank gilt Herrn Peter Ewert für die Betreuung, Herrn Christian Meierhofer für das Mentoring und Herrn Sohrab Fratz für die Konzeption dieser Arbeit.

Sehr herzlich bedanken möchte ich mich ebenfalls bei Frau Judith Zimmermann, Frau Kristina Belker, Frau Anja Hennemuth, Frau Naira Mkrtchyan, Herrn Heiko Stern und Herrn Heiner Latus für die wissenschaftliche Unterstützung.